Covariability of Surface Wind and Stress Responses to Sea Surface Temperature Fronts

Larry W. O'Neill

College of Earth, Ocean, and Atmospheric Sciences, Oregon State University, Corvallis, Oregon

Dudley B. Chelton

*College of Earth, Ocean, and Atmospheric Sciences, and Cooperative Institute for Oceanographic Satellite Studies,
Oregon State University, Corvallis, Oregon*

Steven K. Esbensen

College of Earth, Ocean, and Atmospheric Sciences, Oregon State University, Corvallis, Oregon

ABSTRACT

The responses of surface wind and wind stress to spatial variations of sea surface temperature (SST) are
investigated using satellite observations of the surface wind from the Quick Scatterometer (QuikSCAT) and
SST from the Advanced Microwave Scanning Radiometer on the Advanced Microwave Scanning Radiom-
eter for Earth Observing System (EOS) (AMSR-E) *Aqua* satellite. This analysis considers the 7-yr period
June 2002–May 2009 during which both instruments were operating. Attention is focused in the Kuroshio,
North and South Atlantic, and Agulhas Return Current regions. Since scatterometer wind stresses are
computed solely as a nonlinear function of the scatterometer-derived 10-m equivalent neutral wind speed
(ENW), qualitatively similar responses of the stress and ENW to SST are expected. However, the responses
are found to be more complicated on the oceanic mesoscale. First, the stress and ENW are both approxi-
mately linearly related to SST, despite a nonlinear relationship between them. Second, the stress response to
SST is 2 to 5 times stronger during winter compared to summer, while the ENW response to SST exhibits
relatively little seasonal variability. Finally, the stress response to SST can be strong in regions where the
ENW response is weak and vice versa.

A straightforward algebraic manipulation shows that the stress perturbations are directly proportional to the
ENW perturbations multiplied by a nonlinear function of the ambient large-scale ENW. This proportionality
explains why both the stress and ENW depend linearly on the mesoscale SST perturbations, while the de-
pendence of the stress perturbations on the ambient large-scale ENW explains both the seasonal pulsing and the
geographic variability of the stress response to SST compared with the less variable ENW response.

1. Introduction

Satellite and in situ measurements of surface wind
stress and sea surface temperature (SST) show a strong
coupling and positive correlation on spatial scales of
100–1000 km (see reviews by Small et al. 2008; Chelton
and Xie 2010), which are classified as mesoα and mesoβ
scales according to the Orlanski (1975) classification.

SST perturbations associated with a variety of mesoscale
oceanic phenomena, including eddies, ocean current
meanders, upwelling regions, and quasi-permanent SST
frontal zones, induce perturbations in the surface wind
stress, with enhanced stress over warm water and re-
duced stress over cooler water; on the oceanic meso-
scale, the ocean thus drives an atmospheric response, in
contrast to what occurs over much larger spatial scales
($\gtrsim$1000 km; e.g., Frankignoul 1985; Cayan 1992; Mantua
et al. 1997; Okumura et al. 2001; Xie 2004).

One hypothesis for what causes the surface wind stress
response to mesoscale SST variability involves the mod-
ification of surface stability, which can modify the surface

Corresponding author address: Larry W. O'Neill, College of
Earth, Ocean, and Atmospheric Sciences, Oregon State Univer-
sity, 104 COAS Administration Building, Corvallis, OR 97331.
E-mail: loneill@coas.oregonstate.edu

wind stress independent of wind speed. A recent analysis of moored buoy observations near the Gulf Stream and equatorial Pacific cold tongue, however, shows that stability variations alone can only account for 10%–30% of the stress response to SST (O'Neill 2012); the surface stress response to SST is thus primarily a consequence of the response of the surface wind speed to SST, consistent with earlier studies based on numerical models and sensitivity analyses (e.g., Small et al. 2003; O'Neill et al. 2005; Small et al. 2008; Song et al. 2009). Surface wind speed changes across SST fronts have been at least qualitatively observed from in situ observations (e.g., Sweet et al. 1981; Jury and Walker 1988; Hayes et al. 1989; Mey et al. 1990; Bond 1992; Friehe et al. 1991; Jury 1994; Kudryavtsev et al. 1996; Rouault and Lutjeharms 2000; Anderson 2001; Thum et al. 2002; Hashizume et al. 2002; Bourras et al. 2004; Raymond et al. 2004; Mahrt et al. 2004; Tokinaga et al. 2005; Pezzi et al. 2005).

To fully account for the surface stress response to SST, the surface wind speed response to SST must thus be considered. Observational and modeling studies have shown that mesoscale SST variations cause surface wind perturbations through intermediary responses of the marine atmospheric boundary layer (MABL) pressure and turbulence fields to SST-induced surface heating perturbations (for a thorough review, see Small et al. 2008). Briefly, these studies demonstrate that mesoscale SST variability drives perturbations in surface heat fluxes, which in turn significantly modify MABL pressure gradient and vertical turbulent stress divergence fields. Thermally induced hydrostatic pressure gradients form within the MABL, with lower pressure over warmer SSTs and higher pressure over cooler SSTs (e.g., Lindzen and Nigam 1987; Cronin et al. 2003; Small et al. 2003), although this effect may be counteracted somewhat by changes in MABL depth (e.g., Hashizume et al. 2002).

Variations in the vertical turbulent stress divergence near SST fronts include the effects of 1) vertical turbulent mixing of momentum driven by surface heating variations across SST fronts, which enhances momentum transport from aloft to the surface over warmer SSTs compared to cooler SSTs (e.g., Sweet et al. 1981; Jury and Walker 1988; Wallace et al. 1989; Hayes et al. 1989; Wai and Stage 1989; Bond 1992; de Szoeke and Bretherton 2004; Song et al. 2009; O'Neill et al. 2010b); 2) surface friction perturbations opposing the SST-induced pressure gradient–driven flow (Small et al. 2005b, 2008; O'Neill et al. 2010b); and 3) variations in the depth of the momentum boundary layer, which in equilibrium occur as the surface stress balances the large-scale pressure gradient (Samelson et al. 2006; Spall 2007b).

These complicated adjustment processes involving both pressure and turbulent stress ultimately yield the deceptively simple coupling between the surface wind stress and SST observed by satellite. It is emphasized that the results presented in this study are not explicitly dependent upon any particular adjustment mechanism.

Before the availability of satellites capable of measuring surface winds and SST, in situ observations clearly showed that the MABL and surface winds respond strongly to mesoscale SST variability. The earliest of these studies include aircraft observations by Sweet et al. (1981), aircraft and surface-based measurements during the Frontal Air-Sea Interaction Experiment (FASINEX) (Rogers 1989; Friehe et al. 1991), ship-based in situ and microwave radar observations along the Gulf Stream (Kudryavtsev et al. 1996), ship-based and aircraft observations along the Agulhas Current region south of Africa (Jury and Walker 1988; Mey et al. 1990; Jury 1994), aircraft observations over the Azores during the Structure des Echanges Mer-Atmosphère, Propriétés des Hétérogénéités Océaniques: Recherche Expérimentale (SEMAPHORE) experiment (Kwon et al. 1998), atmospheric soundings over the equatorial Pacific (Bond 1992), ship-based observations in the Denmark Strait (Vihma et al. 1998), ship-based observations during the Programme Océan Multidisciplinaire Méso Echelle (POMME) in the northeast Atlantic described in Bourras et al. (2004), and buoy observations along the Equatorial Pacific cold tongue (Hayes et al. 1989). While these studies are of enormous benefit, their limited durations and spatial extents preclude the investigation of seasonal and geographic variability. Two early experiments by Weissman et al. (1980) and Li et al. (1989) pioneered the use of aircraft-mounted scatterometers to show surface wind stress variations across SST fronts consistent with in situ observations.

Recent progress in understanding the mesoscale influence of SST on surface winds has been motivated by satellite observations of surface winds in regions replete with mesoscale SST variability. In the Northern Hemisphere, these regions include the Kuroshio in the northwest Pacific (e.g., Nonaka and Xie 2003; Liu and Xie 2008; Xu et al. 2010), the Gulf Stream in the northwest Atlantic (e.g., Weissman et al. 1980; Park and Cornillon 2002; Park et al. 2006; Song et al. 2006; Minobe et al. 2008; Xie et al. 2010), and the western Arabian Sea (Vecchi et al. 2004). The equatorial cold tongue in the eastern Pacific Ocean has also garnered significant attention (e.g., Xie et al. 1998; Liu et al. 2000; Chelton et al. 2001; Hashizume et al. 2001; Polito et al. 2001; Zhang and Busalacchi 2009). In the Southern Hemisphere, focus has been on the entire Southern Ocean (O'Neill et al. 2003; White and Annis 2003) and regionally in the Brazil–Malvinas Confluence region (Tokinaga et al. 2005; Pezzi
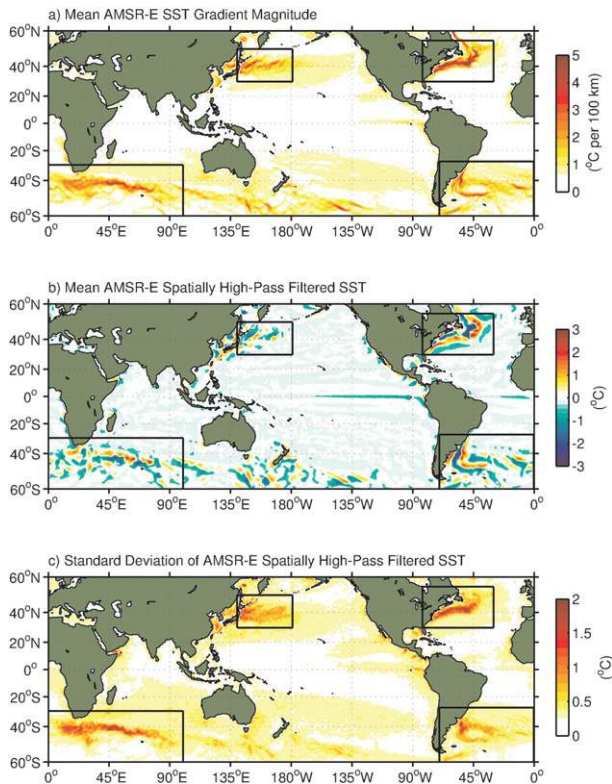
FIG. 1. Maps over the 7-yr period June 2002–May 2009: (a) mean unfiltered AMSR-E SST gradient magnitude; (b) mean spatially high-pass-filtered AMSR-E SST; (c) standard deviation of monthly-averages of spatially high-pass-filtered AMSR-E SST. The four regions investigated in this analysis are enclosed within the rectangles.

et al. 2005), the Agulhas Return Current (ARC) (O'Neill et al. 2005; Liu et al. 2007; Song et al. 2009; O'Neill et al. 2010a), and the Agulhas Retroflection off the southern coast of Africa (Rouault and Lutjeharms 2000). These studies all show positive correlations between surface wind stress and SST on the oceanic mesoscale consistent with in situ observations.

Motivated in part by these previous studies, four extra-tropical regions are chosen as subjects of this study: the Kuroshio Extension, the Gulf Stream region of the North Atlantic, the Brazil–Malvinas Confluence and Zapiola Gyre regions of the South Atlantic, and a region of the Southern Ocean centered on the Agulhas Return Current. These choices are further motivated by the map in Fig. 1a of the SST gradient magnitude averaged over the 7-yr period June 2002–May 2009 derived from the Advanced Microwave Scanning Radiometer for Earth Observing System (EOS) (AMSR-E) Aqua satellite (see section 2). SST gradients are strong and persistent in these long-term time averages over these four midlatitude regions.

In this analysis, we describe the observed covariability between the surface wind and SST on the oceanic mesoscale using satellite wind and SST observations made by the Quick Scatterometer (QuikSCAT) and AMSR-E, respectively. These satellite datasets, along with the time averaging and spatial high-pass filtering used here, are described in section 2. In section 3, the responses of the spatially high-pass-filtered wind stress magnitude and ENW to SST are described empirically, revealing several confusing aspects of the covariability between the wind stress, ENW, and SST. These paradoxes are resolved in section 4, the main analytical piece of this study, which shows how the time-averaged and spatially high-pass-filtered wind stress and ENW are related. This analysis yields several new insights into the contributing factors of the geographical and temporal variability of the response of the wind stress to SST on the oceanic meso-scale. The conclusions and a brief discussion of these results are presented in section 5.

2. Description of satellite observations

For this investigation, we used satellite surface winds from National Aeronautics and Space Administration (NASA)'s QuikSCAT and SST from the AMSR-E Aqua satellite, both of which provide near-global coverage in nonprecipitating conditions. The 7-yr analysis period is June 2002–May 2009, beginning with the 1 June 2002 start of the AMSR-E data record. The spatial resolution of the QuikSCAT wind and AMSR-E SST measurements is about 25 and 56 km, respectively, and both are gridded onto the same 0.25° spatial grid. The Remote Sensing Systems (RSS) version-4 QuikSCAT and version-7 AMSR-E datasets were used, which were the most recent versions at the time of writing.

The spatial resolution of the individual satellite observations restricts our analysis to length scales longer than approximately 50 km. Although the detailed wind response on smaller scales may differ (e.g., Kudryavtsev et al. 1996; Skyllingstad et al. 2006), this study is restricted to assessment of the influence of SST on surface winds on spatial scales longer than the ~50-km footprint of the AMSR-E SST observations. In any case, the larger scales that are resolved by this satellite data are important for ocean forcing (e.g., Milliff et al. 1996; Pezzi et al. 2004; Seo et al. 2007; Spall 2007a; Seo et al. 2008; Jin et al. 2009; Hogg et al. 2009; Zhang and Busalacchi 2009) and can be used to evaluate simulations of the MABL from numerical weather prediction models, either coupled or uncoupled to the ocean (e.g., Chelton and Schlax 2003; Chelton 2005; Maloney and Chelton 2006; Spall 2007b; Seo et al. 2007; Haack et al. 2008; Song et al. 2009; O'Neill et al. 2010b).

a. QuikSCAT scatterometer estimates of surface winds

Scatterometers such as QuikSCAT emit pulses of microwave radiation and measure its backscatter from gravity–capillary waves on the sea surface. For geophysical remote sensing purposes, one of the most interesting aspects of microwave radar returns from gravity–capillary waves is a systematic variation of backscatter intensity with wind speed and direction. Rice (1951) showed that radar returns from adjacent crests of wind-driven centimeter-scale surface waves add in phase, thus forming the basic principal of the Bragg resonance condition relating microwave backscatter to wind ripples on the sea surface. This idea was confirmed and further developed in wind–wave systems by Crombie (1955) and Wright (1966), among others. Later studies showed that gravity–capillary waves in the ocean grow as a function of the surface wind stress (e.g., Pierson and Stacy 1973; Mitsuyasu and Honda 1974), which completed the link between microwave radar backscatter and surface wind stress.

The precise quantity measured by scatterometers is the normalized radar cross section per unit area, which is denoted as σ^0. Despite considerable effort, there is currently no known analytical expression between σ^0 and surface wind stress (or friction velocity) sufficient to accurately determine surface winds from σ^0. Surface winds are thus inferred empirically from scatterometer measurements of σ^0 (at various sensor viewing geometries, frequencies, and polarizations) using a geophysical model function (GMF) developed from in situ wind measurements (referenced to 10-m height and neutral stability, as discussed below) collocated in space and time with scatterometer σ^0 measurements. Since it is known that σ^0 responds more directly to the surface wind stress (e.g., Jones and Schroeder 1978; Ross et al. 1985; Weissman et al. 1994), it would be most physically consistent to develop a GMF for stress. This approach was taken, for instance, by Weissman et al. (1994) and Weissman and Graber (1999), who developed GMFs for friction velocity for an aircraft Ku-band scatterometer and the spaceborne NASA scatterometer (NSCAT) instrument, respectively.

While this approach to developing a scatterometer GMF is most consistent with the physics of the wind-roughened sea surface, the relative lack of in situ surface stress measurements over the ocean (usually from ship-based turbulent velocity measurements) precludes robust GMF development in terms of stress. Instead, QuikSCAT GMF's, including the one used here (based on the Remote Sensing Systems Ku-2011 GMF; L. Ricciardulli and F. Wentz 2012, personal communication), are formulated in terms of the 10-m equivalent neutral wind

(ENW). The ENW is a reference wind speed at 10-m height that would exist for a given surface wind stress if the near-surface atmosphere were neutrally stratified, the surface motionless, and using the in situ friction velocity and momentum roughness length (e.g., Ross et al. 1985; Liu and Tang 1996). The ENW can be thought of as a reference wind in much the same way that potential temperature can be thought of as a reference temperature.

GMFs are developed for ENWs rather than the actual in situ surface winds because scatterometer σ^0 measurements depend on the surface wind stress. The surface wind stress depends not only on the actual surface wind speed, but also on surface stability, which scatterometers cannot measure. This stability dependence is removed in the ENW, which is referenced to neutral stability, and the surface stress can be estimated directly from it.

The QuikSCAT wind stress magnitude $|\tau|$ is estimated from the ENW V_n, using the standard bulk formulation

$$|\tau| = \rho_0 C_{d10n} V_n^2, \tag{1}$$

where ρ_0 is the surface air density (considered as a constant equal to 1.22 kg m^{-3}), and C_{d10n} is the 10-m neutral stability drag coefficient. Several parameterizations for C_{d10n} are in common use, and there is no consensus as to which is most accurate. The neutral drag coefficient C_{d10n} used here is based on the formulation used in the Coupled Ocean–Atmosphere Response Experiment, version 3.0 (COARE 3.0) bulk flux algorithm (Fairall et al. 2003), which is the most up-to-date formulation currently available. As with most C_{d10n} parameterizations, it varies as a function of the ENW (solid curve, Fig. 2). A continuous analytical approximation for C_{d10n} suitable for our purposes here is obtained by fitting the following function to the COARE C_{d10n}:

$$C_{d10n} = \frac{a_0}{V_n} + b_0 + c_0 V_n, \tag{2}$$

where $a_0 = 0.45 \times 10^{-3}$ m s^{-1}, $b_0 = 0.57 \times 10^{-3}$, and $c_0 = 0.07 \times 10^{-3}$ m^{-1} s. This fit is shown in Fig. 2a along with the C_{d10n} from Large et al. (1994) that is often used to compute wind stress from scatterometer ENW. More detailed comparisons of QuikSCAT wind stresses estimated from frequently used neutral drag coefficient parameterizations are shown in the appendix of Risien and Chelton (2008). As shown in Fig. 2a, for an ENW above about 6 m s^{-1}, the COARE C_{d10n} is about 15% larger than from Large et al. (1994), although above 7 m s^{-1}, both increase at the same rate with increasing ENW. Combining Eqs. (1) and (2), the QuikSCAT $|\tau|$ can thus be estimated as a cubic polynomial function of the QuikSCAT V_n:
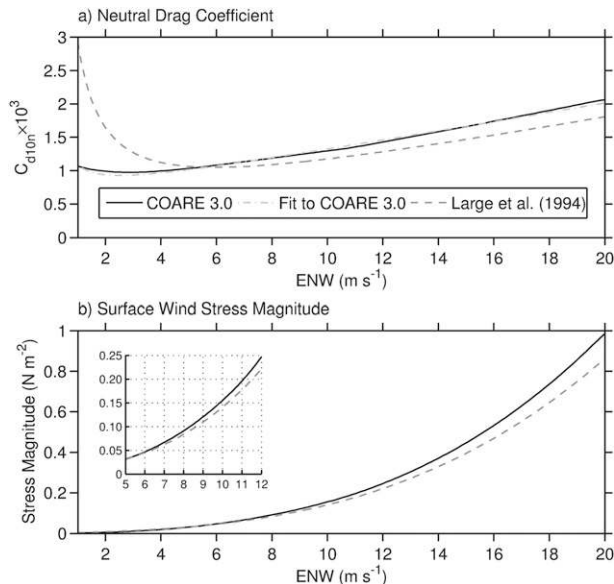
FIG. 2. (a) Dependence of the 10-m neutral stability drag coefficient C_{d10n} on the ENW from COARE 3.0 (solid; Fairall et al. 2003), appendix A of Large et al. (1994) (dashed), and the form used in this analysis (dashed-dot), which as discussed in the text, consists of a curve fitted to the COARE neutral drag coefficient using Eq. (2). (b) The surface wind stress magnitude as a function of the ENW computed using Eq. (1) and the neutral drag coefficients from COARE 3.0 (black) and Large et al. (1994) (dashed). The inset magnifies the wind stress in the range of ENW from 5 to 12 m s^{-1}.

$$|\tau| = \rho_0(a_0 V_n + b_0 V_n^2 + c_0 V_n^3). \qquad (3)$$

The resulting stress estimates from the COARE and Large et al. (1994) C_{d10n} as a function of the ENW are shown in Fig. 2b.

Uncertainties in the stress formulation and the neutral drag coefficient are thought to be due to possible effects of fetch, wind steadiness, and statistical homogeneity, all of which obscure the true relationships in the experimental data in which these parameterizations are based (e.g., Garratt 1977). Additionally, nonlocally generated surface swell can decouple the surface winds from the surface stress (e.g., Geernaert 1990; Large et al. 1995; Bourassa et al. 1999), which cannot easily be accounted for using current wind stress parameterizations. Despite these uncertainties, the formulation provided by Eq. (1) is generally how the surface wind stress is estimated over the ocean in lieu of direct turbulence measurements.

The estimation of the wind stress also clearly depends on the specification of the surface air density. To assess the sensitivity to the use of a constant air density, the analysis presented in the later sections was repeated using a temporally and spatially varying air density

(appendix A); since these results differed little from what is presented here, we proceed with a constant air density for simplicity.

RMS uncertainties of individual QuikSCAT ENW measurements relative to those derived from in situ observations have been determined from several previous studies (e.g., Ebuchi et al. 2002; Bourassa et al. 2003; Pickett et al. 2003; Chelton and Freilich 2005; Portabella and Stoffelen 2009; O'Neill 2012). In general terms, these studies indicate RMS ENW uncertainties between 1 and 1.7 m s^{-1}. Additionally, ENW uncertainties near strong SST fronts are not significantly different than those in other regions. For instance, RMS differences between individual collocated QuikSCAT and buoy ENW measurements are 1.2 m s^{-1} over the Gulf Stream and 0.9 m s^{-1} over the equatorial Pacific (O'Neill 2012).

b. Time averaging and spatial filtering

Synoptic weather variability unrelated to the SST influence on surface winds investigated here, and to a lesser extent, random measurement uncertainties, were mitigated by averaging the wind and SST fields at monthly intervals. To further isolate the mesoscale SST influence on surface winds, we spatially high-pass filtered the satellite wind and SST fields to remove spatial variability with wavelengths longer than 10° latitude by 20° longitude using a two-dimensional loess smoother (Cleveland and Devlin 1988; Schlax and Chelton 1992). This filtering has smoothing characteristics analogous to a 6° latitude by 12° longitude block average smoother (Schlax et al. 2001). We show in section 3b that this analysis is insensitive to a broad range of filter cutoff wavelengths. Hereafter, fields spatially high-pass filtered in this manner are referred to as perturbation fields. This spatial high-pass filtering removes the negative correlation between surface winds and SST that are known to occur over much larger spatial scales (e.g., Frankignoul 1985; Cayan 1992; Mantua et al. 1997; Okumura et al. 2001; Xie 2004), while also mitigating any coherent large-scale measurement biases.

A map of the 7-yr mean AMSR-E SST perturbation field spatially high-pass filtered in this manner is shown in Fig. 1b. These SST perturbations have ranges of ±3°C over the North Atlantic, ±2°C over the South Atlantic and Agulhas regions, and ±1.5°C over the Kuroshio. On monthly time scales, the SST perturbations are most variable along the main oceanic frontal zones in each region, as indicated by a map of the perturbation SST standard deviation shown in Fig. 1c. The standard deviations are largest along the Agulhas and Gulf Stream, with values exceeding 1.5°–2°C. In the South Atlantic, the perturbation SST is most variable
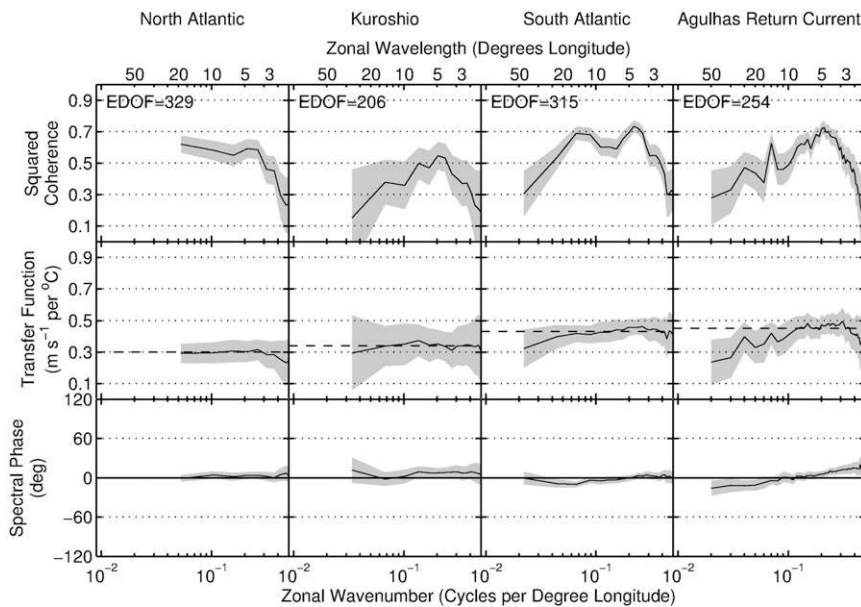
FIG. 3. Cross-spectral statistics of the QuikSCAT ENW and AMSR-E SST as functions of zonal wavenumber: (top) squared coherence, (middle) transfer function, and (bottom) spectral phase. The four regions of interest here are noted above each column of panels. These statistics were computed from monthly averaged QuikSCAT ENW and AMSR-E SST fields over the period June 2002–May 2009. Only cross-spectral statistics where the squared coherences are statistically significant above the 95% confidence level are shown, and 95% confidence intervals of the statistics are shown by the gray shading in each panel (estimated according to p. 317 in Bendat and Piersol 1986). Estimates of the equivalent degrees of freedom (EDOF) of the cross-spectral estimates are shown in each column of panels. The corresponding zonal wavelengths in degrees longitude are shown at the top of the figure. The dashed horizontal lines in the middle row of panels are the slopes of the regression lines for the binned scatterplots in Figs. 4–7 for the spatially high-pass-filtered ENW and SST.

along the periphery of the Zapiola Gyre and downstream of Drake Passage.

3. Surface wind stress and ENW responses to SST

a. Cross-spectral statistics between ENW and SST

The dependence of the interactions between the ENW and SST on spatial scale is shown here through investigation of cross-spectral statistics (squared coherence, transfer function, and spectral phase) of the unfiltered QuikSCAT ENW and AMSR-E SST as a function of zonal wavenumber for each region (Fig. 3). These were computed from the 7 years of monthly-averaged ENW and SST fields along continuous zonal transects in each region using spectral ENW and SST estimates obtained from a first-difference filter.

The squared coherences are highest for wavenumbers larger than 0.1 cpd (cycles per degree longitude), peaking at zonal wavelengths of roughly 4° longitude. Maximum squared coherences in each region range from ~0.55 over the Kuroshio to ~0.75 over the South Atlantic and Agulhas regions.

The cross-spectral transfer functions (middle row of Fig. 3) show an ENW response to SST that is relatively constant with zonal wavenumber for wavelengths between roughly 3° and 20° longitude. For wavenumbers smaller than about 0.05 cpd (corresponding to zonal wavelengths longer than 20° longitude) where resolved, the squared coherences and transfer functions generally decrease. The transfer functions show that the ENW response to SST is stronger for the South Atlantic and Agulhas regions than for the North Atlantic and Kuroshio regions. These transfer function and squared coherence estimates are consistent with the cross-spectral analysis of satellite wind and SST fields by Small et al. (2005a).

Cross-spectral phases are near zero for all zonal wavenumbers over all regions, as shown in the bottom row of Fig. 3. Over the Agulhas Return Current, there is a small linear trend in the phase, which indicates a zonal offset between ENW and SST over the range of resolved wavenumbers. The zonal offset inferred from the slope of the phase spectra over the Agulhas corresponds to ~0.2° longitude, or about one grid point. This zonal offset is
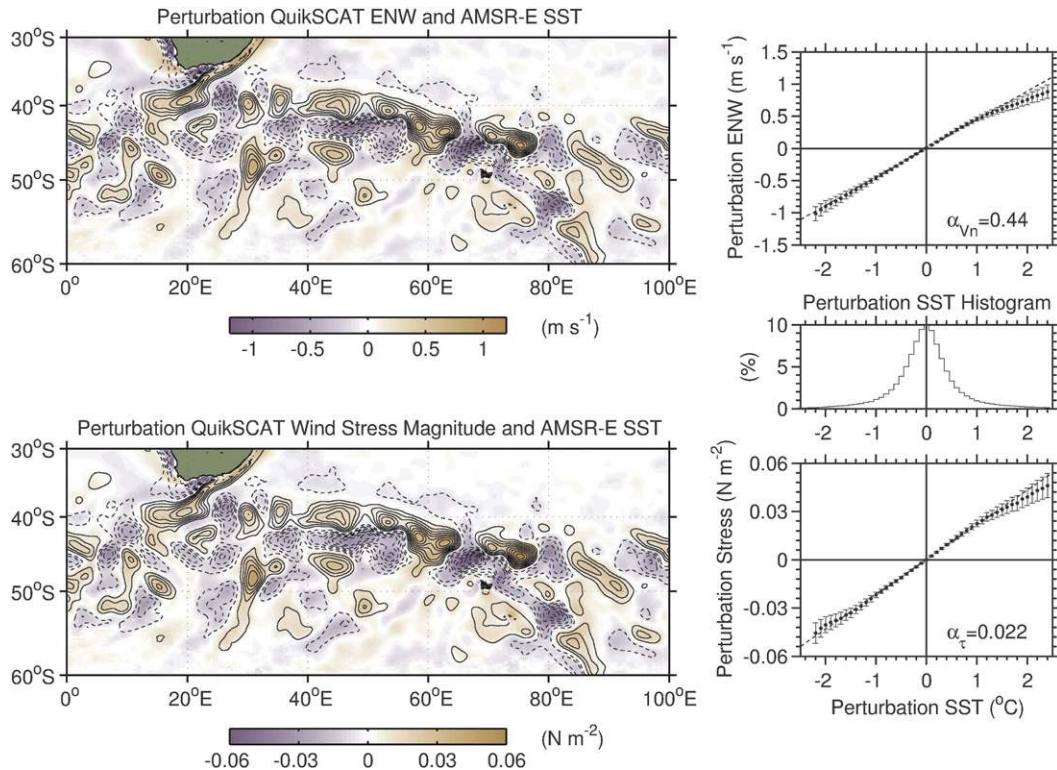
FIG. 4. Maps of the spatially high-pass-filtered (top left) QuikSCAT ENW (colors) and (bottom left) surface wind stress magnitude (colors) averaged over the period June 2002–May 2009 over the Agulhas Return Current region. The contours overlaid in each map are the spatially high-pass-filtered AMSR-E SST averaged over the same period, with dashed (solid) contours representing negative (positive) SST perturbations. The contour interval is 0.25°C, and the zero contour has been omitted for clarity. To the right of these maps are binned scatterplots of the perturbation (top) ENW and (bottom) wind stress magnitude as functions of the perturbation SST computed from the monthly averaged perturbation wind and SST fields over the same 7-yr period. Within each SST bin, the points represent the means of the monthly averaged wind, and the error bars represent estimates of the 95% confidence intervals of the means within each bin computed from a two-sided t interval using an effective degrees of freedom, which accounts for the nonindependence of individual observations. The dashed line in each panel is a least squares fit of the points to straight lines having a slope as indicated in the lower right. (middle right) A histogram of the perturbation SST is shown, also computed from the monthly-averaged perturbation SST fields.

consistent with the spatially lagged cross correlations between spatially high-pass-filtered ENW and SST shown in O'Neill et al. (2005) over the Agulhas region. The near-zero slopes of the phase spectra in the other three regions indicate no significant zonal offset between ENW and SST.

b. Empirical relationships derived from satellite observations

Contours of the spatially high-pass-filtered SST overlaid onto maps of the spatially high-pass-filtered ENW and wind stress magnitude averaged over the 7-yr period June 2002 to May 2009 are shown in Figs. 4–7 for each of the four regions considered here. As in previous studies summarized in the introduction, the wind stress magnitude and ENW perturbations exhibit strong, positive correlations with the SST perturbations, where both

increase over warm SST perturbations and decrease over cool ones. The cross-correlation coefficients between the monthly averaged ENW and SST fields range from 0.56 over the Kuroshio Extension to 0.72 over the South Atlantic (Table 1), while for stress and SST, they are between 0.45 over the Kuroshio and 0.67 over the Agulhas Return Current.

Binned scatterplots of the wind stress and ENW perturbations as a function of the perturbation SST for the 7-yr analysis period (right column of panels, Figs. 4–7) show that both depend approximately linearly on the SST perturbations, such that

$$\overline{|\tau|}' \approx \alpha_\tau \overline{T_s}', \quad \text{and} \tag{4}$$

$$\overline{V_n}' \approx \alpha_{vn} \overline{T_s}', \tag{5}$$
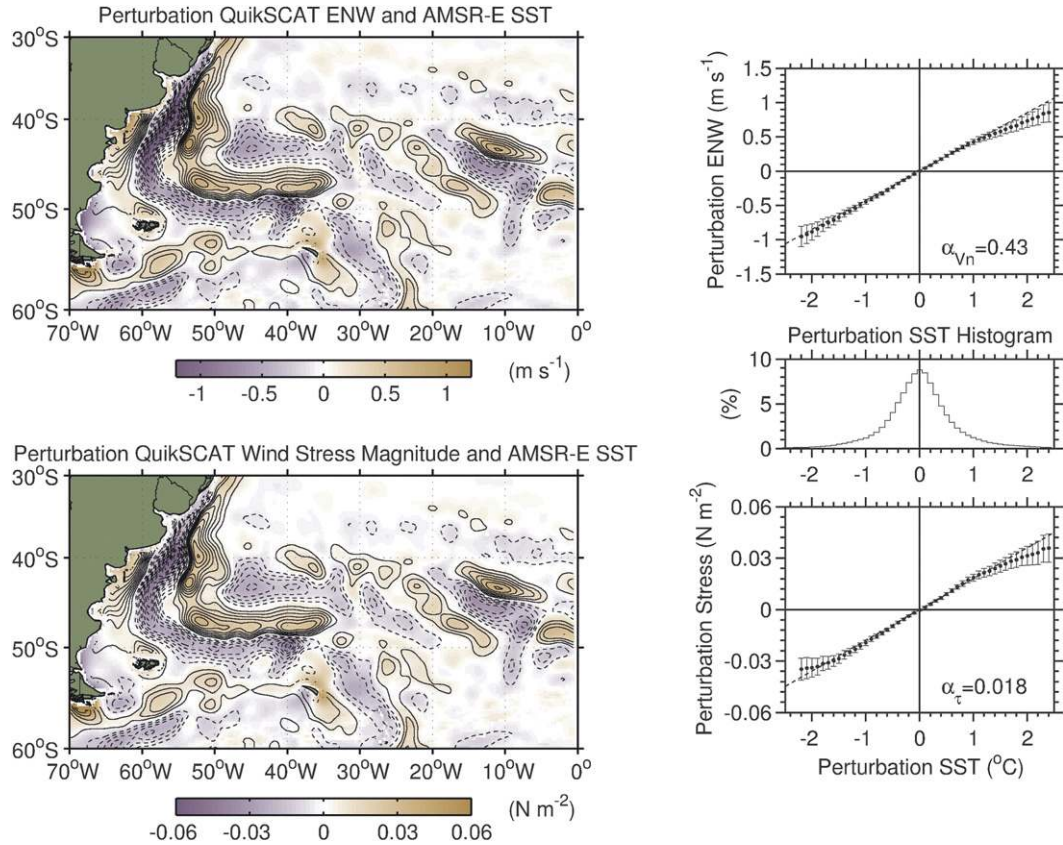
FIG. 5. As in Fig. 4, but for the South Atlantic.

respectively, where T_s is SST, overbars denote monthly averages, and the primes represent spatially high-pass filtered quantities. Thus, $\overline{|\tau|}'$, $\overline{V_n}'$, and $\overline{T_s}'$ represent the monthly averaged and spatially high-pass-filtered wind stress magnitude, ENW, and SST, respectively. The coupling coefficients $\alpha_\tau = \partial\overline{|\tau|}'/\partial\overline{T_s}'$ and $\alpha_{vn} = \partial\overline{V_n}'/\partial\overline{T_s}'$ are the linear slopes computed from regression fits to the binned averages, and provide the means for quantifying the SST influence on surface winds in this analysis. The slopes α_τ and α_{vn} and their 95% confidence intervals, are summarized in Table 1; α_τ and α_{vn} are statistically significant over all regions.

Since the QuikSCAT wind stress was computed solely as a function of the QuikSCAT ENW using Eq. (3), it is not surprising that the stress response to SST varies in a manner similar to the ENW response. However, it is surprising that the stress and ENW are both related linearly to the perturbation SST even though the stress is a nonlinear function of the ENW per Eq. (3). This paradox is reconciled in section 4. In appendix A, we show that the α_τ estimates found here do not depend strongly on specification of the neutral drag coefficient or surface air density.

A consistent feature evident in the binned scatterplots is an apparent flattening of the stress and ENW binned averages for SST perturbations greater than about +1.25°C. At $\overline{T_s}' = +2$°C, this leads to a discrepancy between the binned averages and the regression line of roughly 0.2 m s^{-1}. The significance of this apparent flattening is difficult to assess, however, since there are few observations in the tails of the monthly-averaged perturbation SST distributions, as shown by histograms of $\overline{T_s}'$ (Figs. 4–7). This flattening may just be a statistical artefact of insufficient sampling in the tails of the $\overline{T_s}'$ distribution.

The values of α_{vn} are relatively insensitive to the choice of filter cutoff wavelengths used to spatially high-pass filter the satellite wind and SST fields. To show this, α_{vn} was computed as a function of the zonal and meridional filter cutoff wavelengths (referred to as SPAN_X and SPAN_Y, respectively) for the 2-yr period June 2002–May 2004 (Fig. 8, top row). We chose this shorter period because of the large computational expense of spatially filtering the global ENW and SST fields at monthly intervals. Over all four regions, α_{vn} varies by less than ~25% over the broad range of smoothing half-spans shown here. Halving the filter cutoff wavelengths
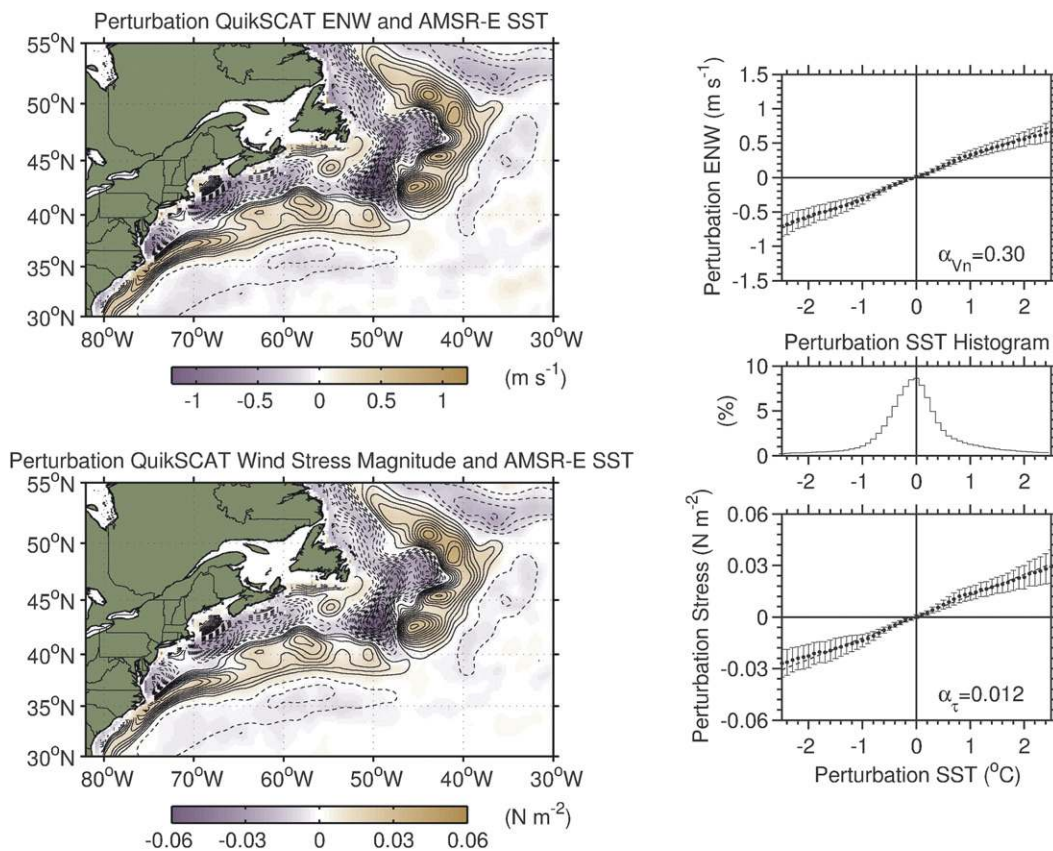
FIG. 6. As in Fig. 4, but for the North Atlantic.

from the 20° longitude by 10° latitude used throughout this analysis to 10° longitude by 5° latitude only changes the α_{vn} estimates by less than 10%. Because of the sharp meridional gradients of SST in these regions, most of the sensitivity of α_{vn} to spatial filtering occurs from the specification of SPAN_Y for SPAN_Y $\lesssim$ 10° latitude, while α_{vn} is relatively insensitive to the full range of SPAN_X considered here. Note that the cross-correlation coefficients between ENW and SST as a function of smoothing parameter (Fig. 8, bottom row) exhibit similar trends to those of α_{vn}, with rapidly decreasing correlations for SPAN_Y $\lesssim$ 10° latitude.

The linear response of the ENW on SST on oceanic mesoscales is consistent with numerous independent analysis methods and observational sources. First, the cross-spectral transfer functions shown in Fig. 3 between the unfiltered ENW and SST fields express the linear response coefficients of ENW and SST as a function of zonal wavenumber independent of spatial high-pass filtering. The α_{vn} estimates computed from the binned scatterplots in Figs. 4–7 agree well with these transfer functions for zonal wavelengths shorter than the filter cutoff wavelength of 20° longitude used here, as shown

by the black dashed lines in Fig. 3 (middle row). Second, we show in appendix A estimates of α_{vn} obtained from combinations of other satellite datasets, including the AMSR-E ENW and SST, the WindSat ENW and SST, and the QuikSCAT ENW and Reynolds optimum interpolation (OI) v2 SST fields. These estimates agree to within 10% of those derived from the QuikSCAT ENW and AMSR-E SST fields shown here. Third, the estimates of α_{vn} are relatively insensitive to large changes in spatial-filtering parameters, as shown in Fig. 8. Finally, the response of the ENW to SST has also been estimated from in situ buoy observations (O'Neill 2012), which show essentially the same linear relationship between the ENW and SST as in the satellite observations analyzed here. The buoy-derived coupling coefficients for the linear ENW response to SST were found to be in good agreement with satellite-derived values. Each analysis thus produces consistent quantitative estimates of α_{vn} independent of observational platform, spatial high-pass filtering, and analysis procedure.

The remainder of this section is devoted to describing the spatiotemporal variability of the stress and ENW responses to SST, which also reveals two other
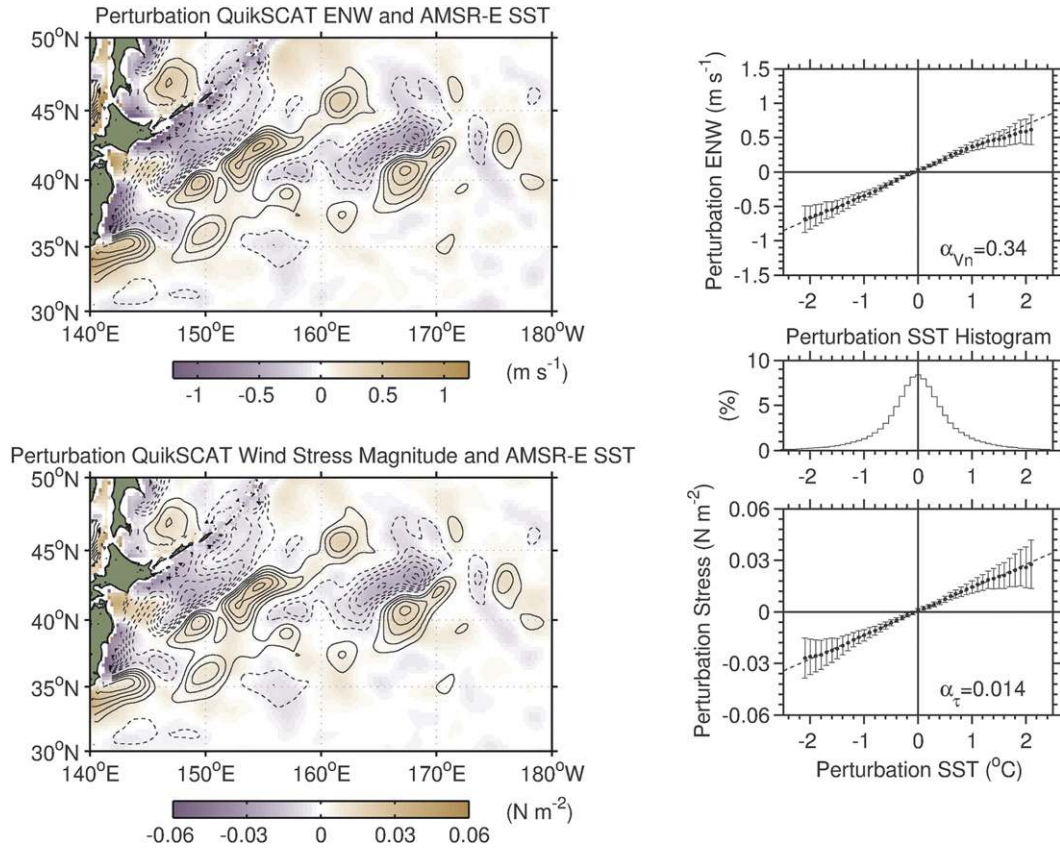
FIG. 7. As in Fig. 4, but for the Kuroshio Extension.

paradoxes regarding the covariability of the stress and ENW responses to SST.

c. Temporal variability of the stress and ENW responses to SST

Time series of α_τ and α_{vn} reveal significant differences in the wind stress and ENW responses to SST (Fig. 9). During winter, α_τ increases by a factor of 2–5 over the Kuroshio and North Atlantic and by 50%–75% over the South Atlantic and Agulhas Return Current compared

to summer (black curves). In contrast, seasonal variability of α_{vn} is much less pronounced (gray curves). There is thus a large seasonal pulsing of the wind stress response to SST that is nearly absent in the ENW response to SST. A similar seasonal pulsing of the SST-induced wind stress response, and lack thereof in the ENW response, has also been observed from buoy observations over the Gulf Stream (O'Neill 2012). In appendix A, we show qualitatively similar seasonal variations of α_τ using two other neutral drag coefficient parameterizations

TABLE 1. Statistics of the mesoscale stress and ENW responses to SST, including the following: the cross-correlation coefficients between the monthly averaged wind stress magnitude $|\tau|'$ and SST $\overline{T_s}'$ and between the ENW $\overline{V_n}'$ and SST; estimates of the coupling coefficients (α_τ, α_{vn}, and β_τ); the ratio $\alpha_\tau/\alpha_{vn} \times 100$; and the medians of the ENW distributions computed from the monthly-averaged QuikSCAT ENW and AMSR-E SST fields over the 7-yr period June 2002–May 2009. Estimates of the 95% confidence intervals are listed for each of the coupling coefficients.

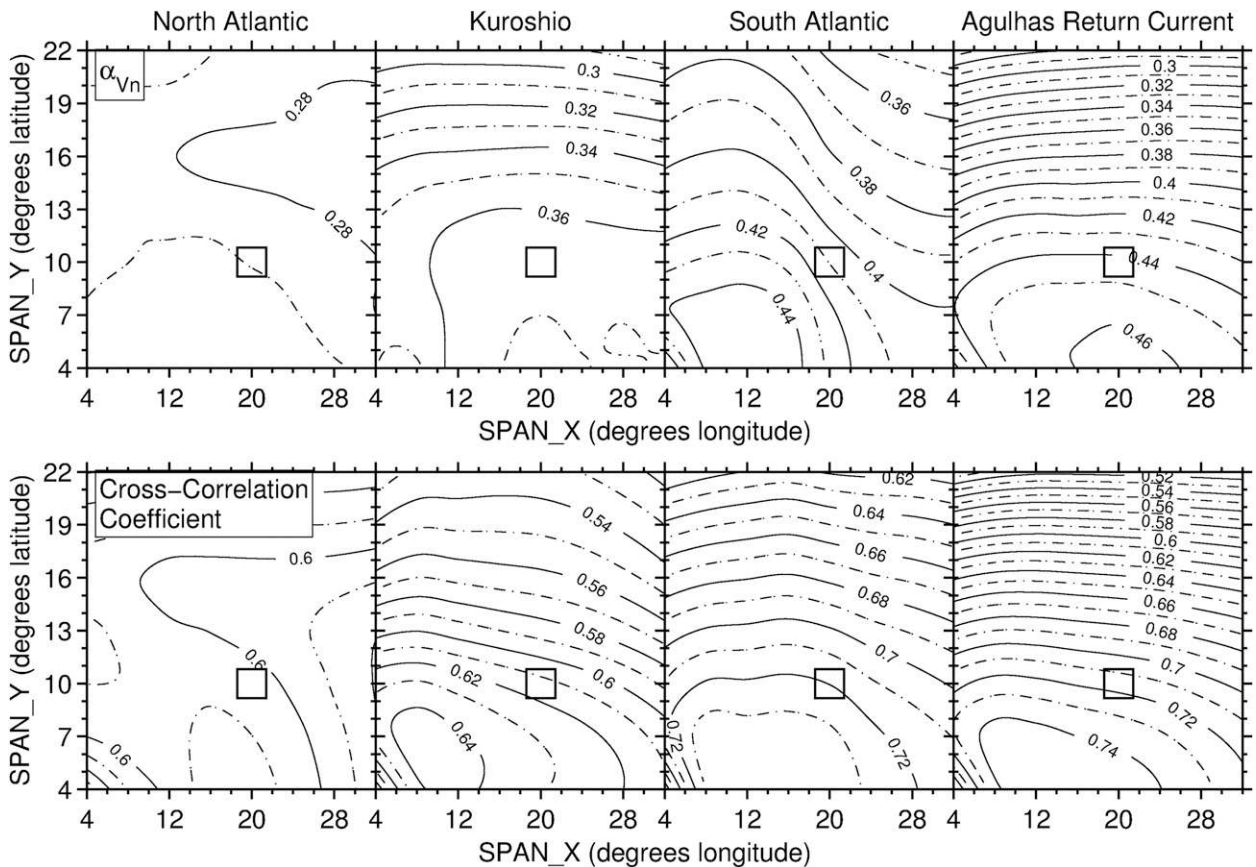| Region	Correlation coefficient with $\overline{T_s}'$		$\alpha_\tau \times 100$ N m^{-2} °C^{-1}	α_{vn} m s^{-1} °C^{-1}	α_τ/α_{vn} $\times 100$	Median ENW m s^{-1}	$\beta_\tau \times 100$ N m^{-2} °C^{-1}
	$|\tau|'$	$\overline{V_n}'$					
Kuroshio	0.45	0.56	1.4 ± 0.2	0.34 ± 0.05	4.1	8.3	0.19 ± 0.03
North Atlantic	0.50	0.62	1.2 ± 0.2	0.30 ± 0.05	4.0	8.3	0.18 ± 0.03
South Atlantic	0.66	0.72	1.8 ± 0.1	0.43 ± 0.03	4.2	8.9	0.29 ± 0.03
Agulhas	0.67	0.71	2.2 ± 0.1	0.44 ± 0.03	4.9	9.9	0.30 ± 0.02

FIG. 8. (top) The coupling coefficient α_{vn} and (bottom) cross-correlation coefficient between the ENW and SST perturbations computed from the monthly-averaged QuikSCAT ENW and AMSR-E SST as a function of the zonal and meridional half-spans of the loess spatial high-pass filter (denoted as SPAN_X and SPAN_Y, respectively; the loess filter was discussed briefly in section 2b). The y axis represents the meridional half-span and the x axis represents the zonal half-span. Because of the computational expense of computing the spatially high-pass-filtered fields, the coupling coefficients were computed only for the 2-yr period June 2002–May 2004 at monthly intervals. The α_{vn} estimates and cross-correlation coefficients were computed from spatially high-pass-filtered ENW and SST fields using an interval of 4° longitude for SPAN_X and 3° latitude for SPAN_Y. The contour interval is 0.01 m s^{-1} °C^{-1} in the top row and 0.01 in the bottom row, and every other contour is dashed–dotted to improve clarity. The SPAN_X of 20° longitude and SPAN_Y of 10° latitude used in this analysis are shown in each panel by the square.

and using a seasonally and spatially varying surface air density.

The seasonal pulsing of the SST-induced wind stress response also exhibits significant interannual variability over all four regions during this 7-yr data record. For instance, the wintertime enhancement of α_τ is reduced by roughly 20% in the winters after 2006/07 over the Kuroshio and is about 25% larger during the winters of 2005/06 and 2006/07 over the North Atlantic.

The wind stress magnitude and ENW perturbations are both well correlated with the SST perturbations year-round, as shown by their cross-correlation time series in Fig. 10 computed at monthly intervals. The cross correlations between the wind stress and SST are slightly lower than those for ENW and SST over all regions. The latter is ~0.6 over the Kuroshio and North Atlantic and ~0.7

over the South Atlantic and Agulhas regions. The correlations are most variable month-to-month over the North Atlantic and least variable over the Southern Hemisphere regions.

Further insight into the covariability between α_τ and α_{vn} is gained by plotting the ratio $\alpha_\tau / \alpha_{vn} \times 100$ as a function of the median unfiltered ENW in each region for each month during the 7-yr analysis record, yielding 84 points for each region (Fig. 11a). There is a strong correspondence between $\alpha_\tau / \alpha_{vn}$ and the median ENW with the ratio ranging between ~1.5 for a median ENW of 5 m s^{-1} to ~7.5 for a median ENW of 12 m s^{-1}, a nearly fourfold increase. For reasons that will become clear in the next section, the ambient large-scale ENW modulates the covariability between α_τ and α_{vn} as implied by this figure.
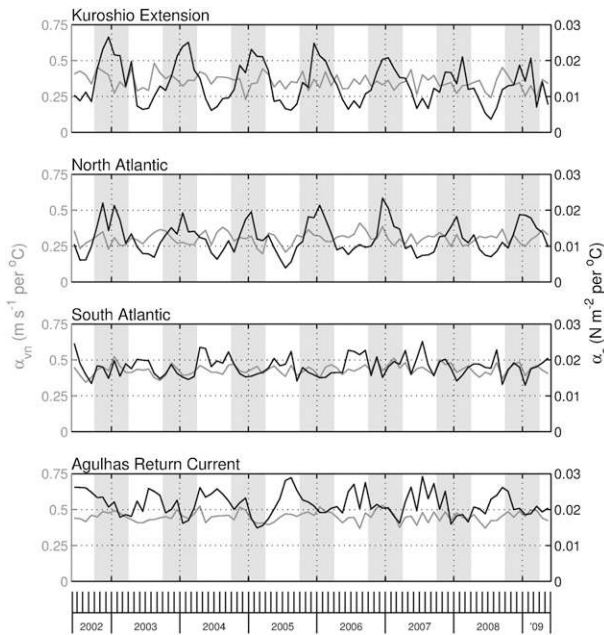
FIG. 9. Time series of the coupling coefficients α_τ (black curves) and α_{vn} (gray curves) computed from the monthly averaged QuikSCAT wind stress and ENW and AMSR-E SST fields for the regions shown in Figs. 4–7.
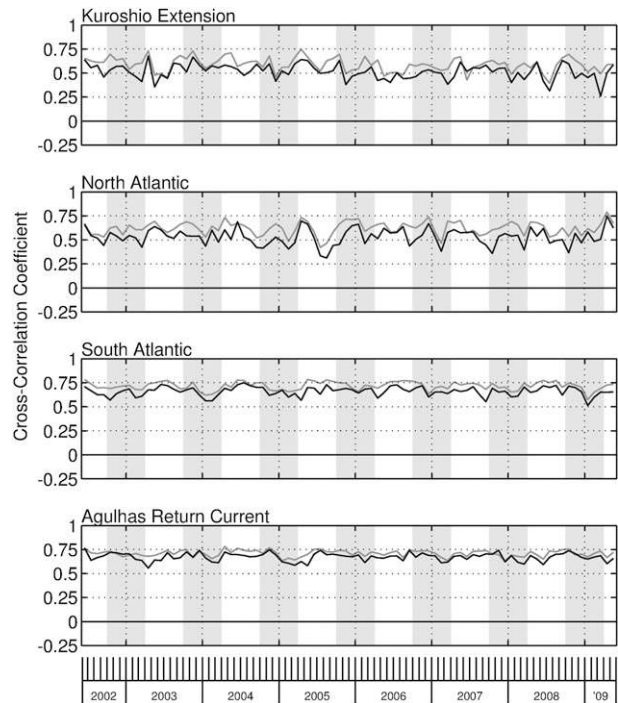

FIG. 10. Time series of the cross-correlation coefficients for the surface wind stress magnitude and SST perturbations (black curves) and ENW and SST perturbations (gray curves) computed from the monthly-averaged QuikSCAT wind and AMSR-E SST fields for the regions shown in Figs. 4–7.

The seasonal pulsing of the mesoscale wind stress field over midlatitudes can also be seen qualitatively from global maps averaged for January 2003–09 (Fig. 12a) and July 2002–08 (Fig. 12b). The wind stress magnitude perturbations nearly vanish during the summer in the Northern Hemisphere (Fig. 12b) and are much smaller during January in the Southern Hemisphere (Fig. 12a) compared to the corresponding winter months. In contrast, the perturbation ENW differences between winter and summer are much less pronounced (Figs. 13a,b). The large seasonal pulsing of the wind stress perturbations, and lack thereof in the ENW perturbations, is consistent with the time series of α_τ and α_{vn} shown in Fig. 9. These time series further show that the seasonal pulsing of the wind stress perturbations is not attributable directly to seasonal variability of the SST perturbations.

d. Geographic variability of the stress and ENW responses to SST

Compared with α_{vn}, the magnitudes of α_τ show little consistency between the four analysis regions (Table 1). These differences are quantified more clearly by computing the ratio $\alpha_\tau/\alpha_{vn} \times 100$, which is listed in Table 1 for each region. This ratio is just over 4 for the North and South Atlantic and Kuroshio regions, and 4.9 for the Agulhas. An important feature of the geographic variability of α_τ/α_{vn} is that it is largest where the median

unfiltered ENW is largest, and smallest where the median unfiltered ENW is smallest, as shown in Fig. 14 and Table 1.

Just how variable are α_τ and α_{vn} within each region? To answer this question, α_τ and α_{vn} were computed at each grid point from linear regression of time series of the wind stress magnitude and ENW onto SST at monthly intervals for the 7-yr analysis period. Global maps of the resulting regression estimates of α_τ and α_{vn} are shown in Fig. 15. Areas where the cross correlations are not statistically significant above the 95% confidence level are covered by cross hatching in these maps. Since the majority of points are statistically significant above the 95% confidence level, the mesoscale SST influence on surface winds is a statistically significant feature of the wind field over most of these regions. Areas below this statistical threshold either contain SST surface forcing too weak to generate significant surface wind perturbations in a long-term mean, or are dominated by other persistent mesoscale processes such as topographically forced wind features near coastlines or large-scale convergence zones, among others. While many areas may appear devoid of mesoscale SST variability in this 7-yr mean, propagating eddies with a sufficient SST signature can induce a significant
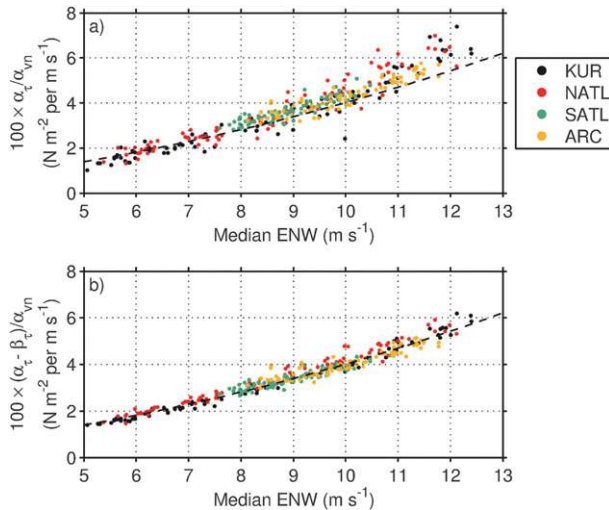
FIG. 11. (a) The ratio $100 \times \alpha_\tau/\alpha_{vn}$ computed from each point in the monthly time series shown in Fig. 9 as a function of the monthly median ENW. Each of the four regions investigated here is color-coded according to the legend in the upper right of the figure. (b) As in (a), but for the ratio $100 \times (\alpha_\tau - \beta_\tau)/\alpha_{vn}$. The dashed curve in (a) and (b) is the function Γ_n computed using the ENW such that $\Gamma_n \approx \rho_0(a_0 + 2b_0 V_n + 3c_0 V_n^2)$. In each plot, there are 84 points for each region, one for each month of the analysis period.
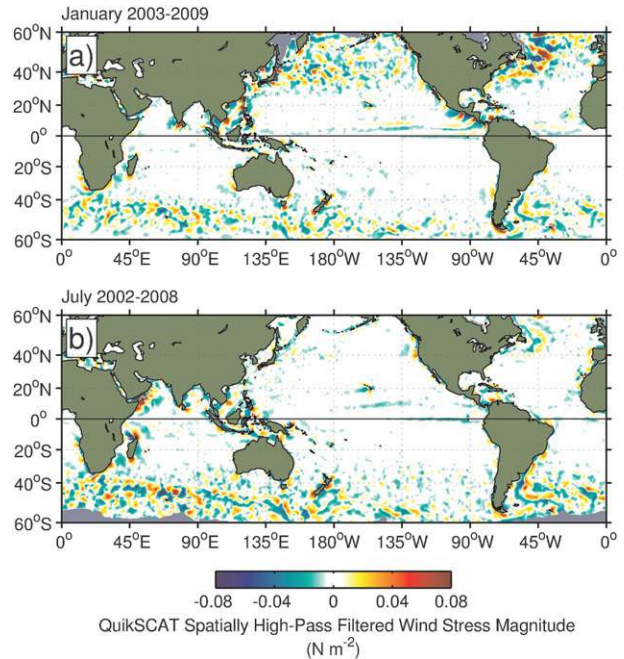

FIG. 12. Global maps of the QuikSCAT spatially high-pass filtered wind stress magnitude for the months of (top) January and (bottom) July during the period June 2002–May 2009. The gray shading in the high-latitude regions represents areas of ice cover present during the specified month for all years.

surface wind response that will not appear in these time-averaged maps due to their transient nature (P. Gaube et al. 2012, personal communication).

Several qualitative features are evident from the global maps of the regression estimates of α_τ and α_{vn} shown in Fig. 15: 1) α_{vn} is greater than zero throughout most of the World Ocean and has a larger magnitude in the Southern Hemisphere compared to the Northern Hemisphere; 2) α_{vn} tends to increase from west to east along the eastward extensions of the western boundary currents of the Kuroshio and Atlantic Ocean; 3) α_τ is largest over mid-latitudes and smallest near ~20° latitude; and 4) α_τ is much more variable across the World Ocean than is α_{vn}; for instance, α_τ is largest over midlatitudes and smallest in the tropics, while α_{vn} is largest in the tropics and smallest along the midlatitude western ocean basins, particularly in the Northern Hemisphere.

Distributions of α_τ and α_{vn} within each region are shown by the histograms in Fig. 15. Also shown by the dashed vertical lines are the values of α_τ and α_{vn} computed from the binned scatterplots in Figs. 4–7, whose values align closely with the medians of these histograms (shown by the gray vertical lines). As Table 2 shows, the standard deviations of the α_τ histograms are between 0.006 and 0.012 N m^{-2} °C^{-1}, while the standard deviations of the α_{vn} histograms are between 0.10 and 0.19 m s^{-1} °C^{-1}, with larger standard deviations over the Southern Hemisphere regions. These histograms confirm

the tendency for larger values of α_τ and α_{vn} in the Southern Hemisphere compared to the Northern Hemisphere. Additionally, they provide a sense of how representative the single area-wide estimates of α_τ and α_{vn} shown in Table 1 are within each region. It is not clear what causes the geographic variability of α_{vn}, although it may be attributable to detailed differences in the large-scale boundary layer structure and coupled processes related to the generation and maintenance of mesoscale SST variability.

4. Relationship between the stress and ENW responses to SST

The differences between the wind stress and ENW responses to SST highlighted in section 3 are puzzling since the wind stress magnitude was computed solely as a function of the ENW. In this section, we demonstrate in a straightforward manner the causes of these differences.

a. Relationship between the monthly averaged wind stress and ENW perturbations

The following simple example provides a qualitative explanation for the differences in the SST-induced wind stress response relative to the ENW response. Consider first a hypothetical SST-induced ENW perturbation of
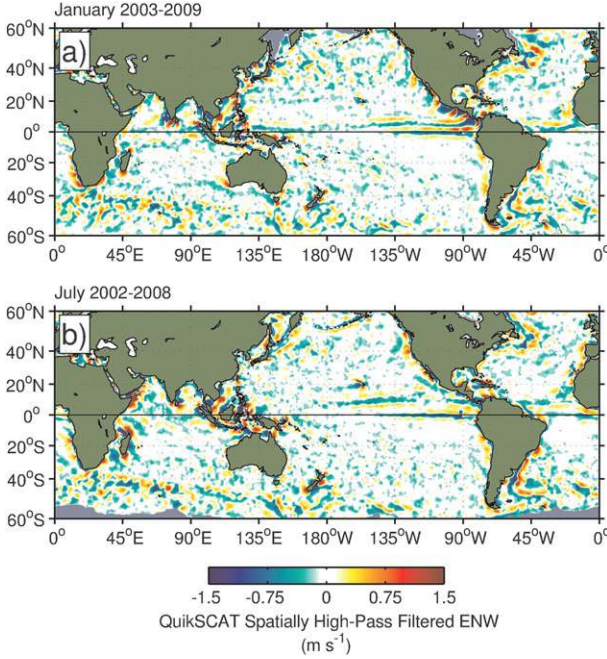
January 2003–2009

July 2002–2008

-1.5 -0.75 0 0.75 1.5

QuikSCAT Spatially High-Pass Filtered ENW
(m s^{-1})

FIG. 13. As in Fig. 12, but for the QuikSCAT spatially
high-pass-filtered ENW.

January 2003–2009

July 2002–2008

0 2 4 6 8 10 12 14

QuikSCAT Unfiltered ENW (m s^{-1})

FIG. 14. As in Fig. 12, but for the QuikSCAT unfiltered ENW.

1 m s^{-1} when the background ENW is 11 m s^{-1}. Using Eq. (3) with an air density of $\rho_0 = 1.22$ kg m^{-3}, the wind stress magnitude difference between 11 and 12 m s^{-1} (where 12 m s^{-1} represents the enhanced ENW over a warm SST perturbation) is 0.051 N m^{-2} (also see the inset of Fig. 2b). Now consider the same 1 m s^{-1} increase in ENW over a warm SST anomaly when the background ENW is 6 m s^{-1}. The increase in wind stress between 6 and 7 m s^{-1} is only 0.021 N m^{-2}. There is thus a factor of ~2.5 difference of the perturbation wind stress for the same hypothetical 1 m s^{-1} ENW perturbation, with the difference owing only to the strength of the background winds.

To isolate the influence of the large-scale winds on the wind stress perturbations more rigorously, it is necessary to consider the effects of the time averaging and spatial filtering applied to the QuikSCAT wind stress and ENW fields in Eq. (3). We do this by partitioning V_n into time-averaged and time-varying components and spatially high-pass- and low-pass-filtered components:

$$V_n = \widetilde{\overline{V_n}} + \overline{V_n}' + \widetilde{V}_n^* + V_n'^*,$$

where overbars represent time-averaged quantities, which here are averaged at 1-month intervals, asterisks represent time-varying components with time scales shorter than 1 month, tildes represent spatially low-pass-filtered fields, and primes represent spatially high-pass-filtered fields. Thus,
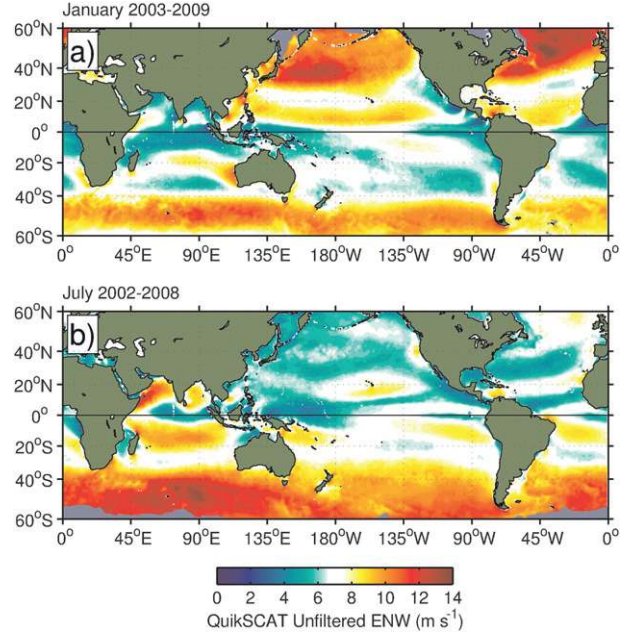
- $\widetilde{\overline{V_n}}$ is the monthly-averaged, spatially low-pass-filtered ENW;
- $\overline{V_n}'$ is the monthly-averaged, spatially high-pass-filtered ENW;
- $\widetilde{V}_n^*$ is the time-varying (on submonthly time-scales), spatially low-pass-filtered ENW; and
- $V_n'^*$ is the time-varying, spatially high-pass-filtered ENW.

Inserting this decomposition into Eq. (3) and simplifying algebraically (see appendix B for more details), the monthly averaged and spatially high-pass-filtered wind stress magnitude $\overline{|\tau|}'$ can be expressed to a close approximation as

$$\overline{|\tau|}' \approx \rho_0\left(a_0 + 2b_0\widetilde{\overline{V_n}} + 3c_0\widetilde{\overline{V_n}}^2\right)\overline{V_n}' \\ + \rho_0\left[(b_0 + 3c_0\overline{V_n})\overline{V_n^{*2}} + c_0\overline{V_n^{*3}}\right]'. \quad (6)$$

The first term on the rhs of this equation shows that $\overline{|\tau|}'$ is directly proportional to $\overline{V_n}'$ multiplied by a nonlinear function of $\widetilde{\overline{V_n}}$, which we refer to in aggregate as the ambient large-scale ENW hereafter. The other term on the rhs of this equation represents the wind stress perturbations generated by temporal variations of ENW on intramonthly time scales. Note that the perturbation stress was not computed with this formula; the total stress was computed using Eq. (3) and spatially high-pass-filtered as discussed at length in section 2. We merely use Eq. (6) to understand and diagnose the relationship between $\overline{|\tau|}'$ and $\overline{V_n}'$.
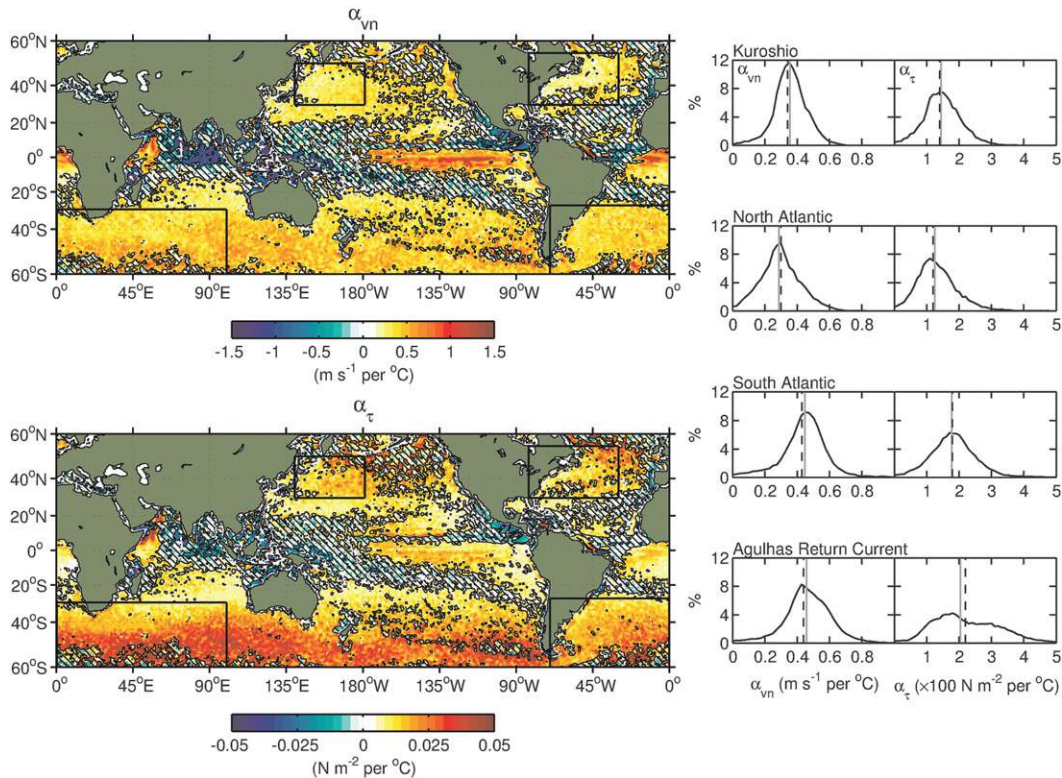
FIG. 15. (left) Global maps of (top) α_{vn} and (bottom) α_τ computed pointwise using least squares linear regression of the monthly averaged QuikSCAT ENW and AMSR-E SST fields over the period June 2002–May 2009. All areas not covered by the crosshatching are statistically significant above the 95% confidence level. (right) Histograms of α_{vn} and α_τ over the four analysis regions enclosed by the boxes. Solid gray vertical lines represent the medians of the histograms, while dashed vertical lines represent the estimates of α_{vn} and α_τ obtained from the binned scatterplots in Figs. 4–7.

b. Covariability between the time-averaged and spatially filtered wind stress, ENW, and SST

Since we have already shown empirically that $\overline{V_n}' \approx \alpha_{vn} \overline{T_s}'$, it immediately follows that the first term on the rhs of Eq. (6) is also related linearly to $\overline{T_s}'$. As we show shortly, this term accounts for most of the wind stress response to SST. The second term on the rhs of Eq. (6) describes contributions to the perturbation wind stress from intramonthly ENW variability. As discussed in appendix B, its existence results from the 1-month averaging applied separately to the wind stress and ENW fields. As shown by the binned scatterplots in Fig. 16 this term satisfies an approximately linear relationship with $\overline{T_s}'$, and is thus represented empirically as

$$\rho_0 \left[(b_0 + 3c_0 \overline{V_n}) \overline{V_n^{*2}} + c_0 \overline{V_n^{*3}} \right]' \approx \beta_\tau \overline{T_s}'.$$

The positive values of the slope β_τ in Fig. 17 indicate that intramonthly ENW variability associated with this term enhances the surface stress over warm SST perturbations and reduces it over cool SST perturbations. Since

β_τ is only 15%–20% of the total value of α_τ (Table 1), this contribution to the SST-induced wind stress response is secondary compared to the SST-induced response of $\overline{V_n}'$ [i.e., the first term on the rhs of Eq. (6)]. The positive correlation of the last term on the rhs of Eq. (6) with $\overline{T_s}'$ is consistent with the results of Sampe and Xie (2007), who found that transient high wind events associated with synoptic weather disturbances are more frequent over warm SST perturbations.

Combining these analytical and empirical results, $\overline{|\tau|}'$ is thus related to $\overline{T_s}'$ by

TABLE 2. Standard deviations of the coupling coefficients α_τ and α_{vn} defined pointwise within the enclosed regions in Fig. 15.

Region	Standard deviation	
	α_τ	α_{vn}
Kuroshio	0.006	0.10
North Atlantic	0.007	0.14
South Atlantic	0.009	0.19
Agulhas	0.012	0.18

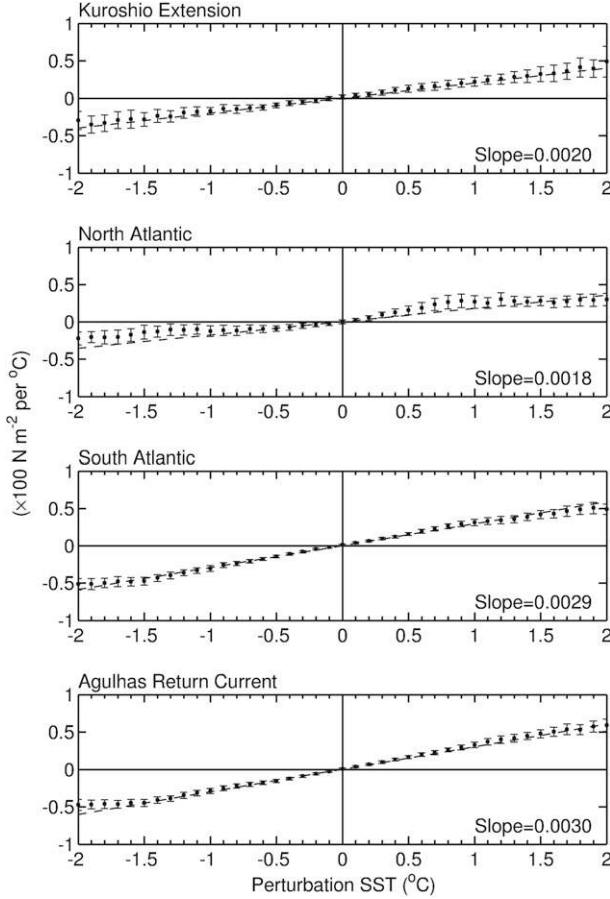FIG. 16. Binned scatterplots of $\rho_0\left[(b_0 + 3c_0\overline{V_n})\overline{V_n^{*2}} + c_0\overline{V_n^{*3}}\right]'$ computed from the monthly averaged QuikSCAT ENW and AMSR-E SST fields. The points represent the means of the monthly-averaged terms within each bin and the error bars represent the 95% confidence intervals of the means within each bin. (bottom right) The slopes of least squares fits of the points to a line are shown and are denoted throughout this analysis as β_τ.

$$\overline{|\tau|}' \approx (\Gamma_n\alpha_{vn} + \beta_\tau)\overline{T_s}', \tag{7}$$

where $\Gamma_n = \rho_0(a_0 + 2b_0\widetilde{\overline{V_n}} + 3c_0\widetilde{\overline{V_n}}^2)$. Comparing Eqs. (4) and (7), α_τ is deduced to be

$$\alpha_\tau \approx \Gamma_n\alpha_{vn} + \beta_\tau. \tag{8}$$

The adequacy of this relationship is confirmed from time series of the left and right sides of this equation, which are very nearly indistinguishable in all regions (Fig. 17).

The effect of the ambient large-scale ENW on the stress response to SST can be further understood by plotting the ratio $(\alpha_\tau - \beta_\tau)/\alpha_{vn}$ (which is approximately equal to Γ_n) as a function of the median ENW for each month and region, as shown in Fig. 11b. Also shown
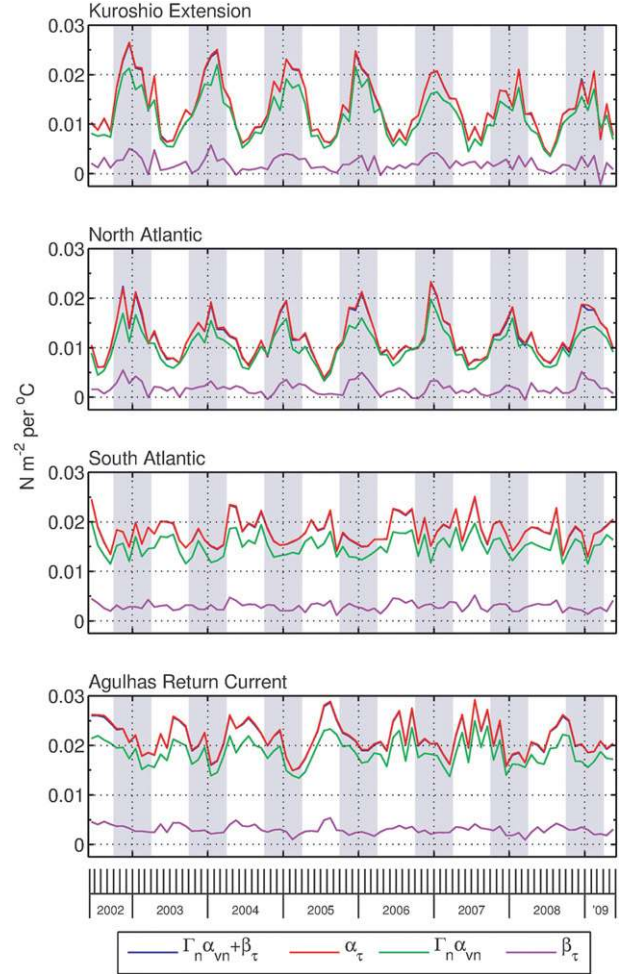

FIG. 17. Time series of the coupling coefficients α_τ (red curves), β_τ (purple curves), and $\Gamma_n\alpha_{vn}$ (green curves) computed from the monthly-averaged QuikSCAT ENW and AMSR-E SST fields over the four analysis regions. The blue curves are the sum of the green and purple curves (i.e., $\Gamma_n\alpha_{vn} + \beta_\tau$) and are shown to confirm the relationship expressed by Eq. (8). Note that the excellent agreement between the blue and red curves makes them difficult to discern.

by the dashed curve is an approximation to Eq. (8): $\Gamma_n \approx \rho_0(a_0 + 2b_0V_n + 3c_0V_n^2)$. The ratio $(\alpha_\tau - \beta_\tau)/\alpha_{vn}$ agrees well with this approximation, which further substantiates the form provided by Eq. (8). The inclusion of β_τ in this ratio significantly reduces the scatter compared with the ratio α_τ/α_{vn} shown in Fig. 11a.

Is it thus apparent from Eq. (8) that the ambient large-scale ENW, acting through Γ_n, modulates α_τ relative to α_{vn}. The strong seasonal pulsing of the SST-induced wind stress perturbations evident in Fig. 9 is thus caused mainly by seasonal variability of the ambient large-scale ENW and hence Γ_n, since seasonal variations of α_{vn} and β_τ in these regions are relatively small (gray and purple
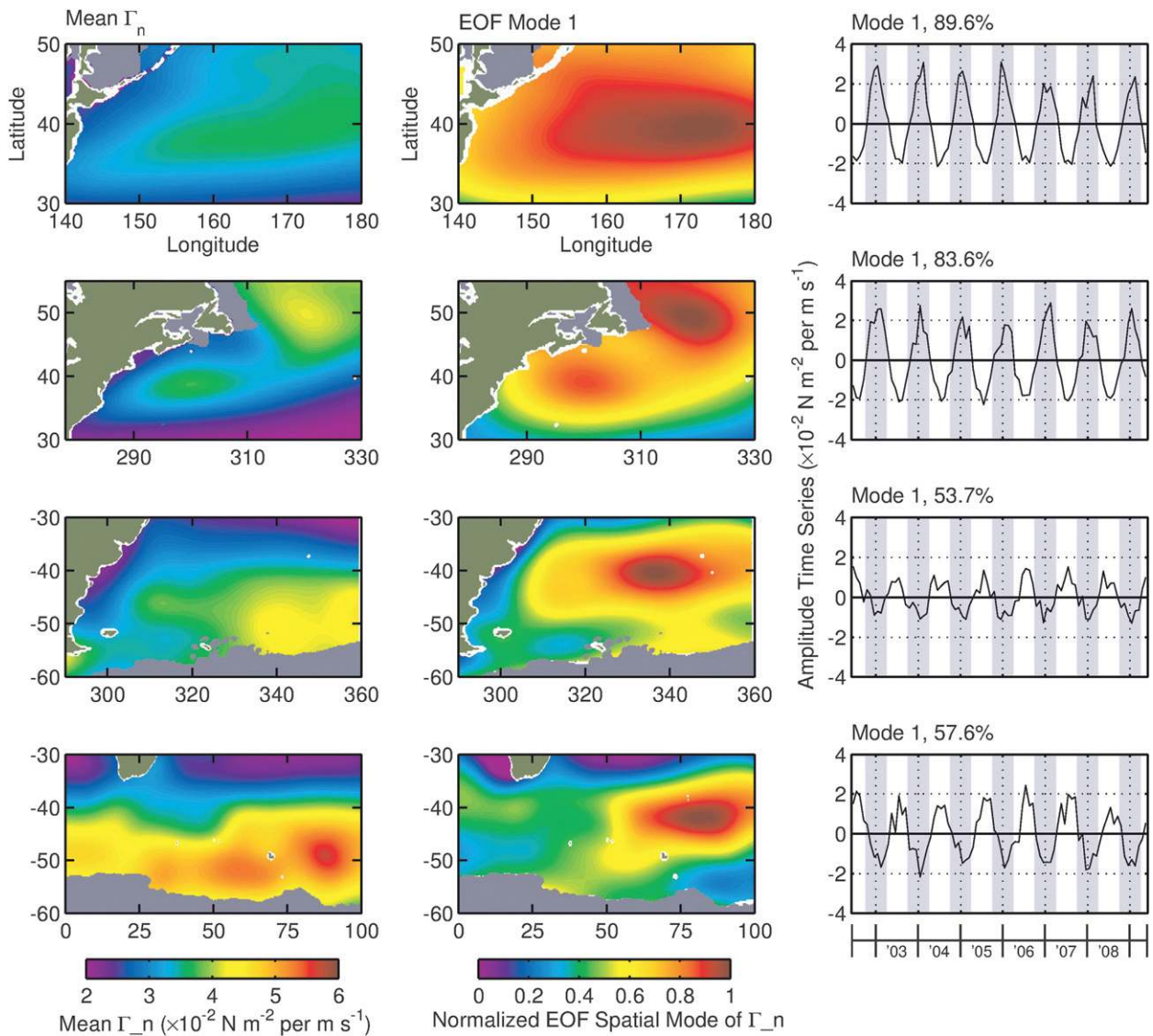
FIG. 18. (left) Maps of the time-averaged Γ_n defined by Eq. (7) for the 7-yr period June 2002–May 2009. Note that the Γ_n fields have been multiplied by 100 and have units of N m^{-2} (m s^{-1})$^{-1}$. (middle and right) First EOF of Γ_n for each region. (middle) Maps of the first normalized spatial mode for each region, and (right) the corresponding amplitude time series are shown. The percentage of variance explained by the first mode EOFs is shown above each panel in the right column. In the maps, the gray overshading denotes any ice-covered regions during the 7-yr analysis period.

curves in Figs. 9 and 17, respectively). Likewise, the geographical variability of α_τ relative to α_{vn} shown in Table 1 and Fig. 15 is attributable mostly to geographical variations of the ambient large-scale ENW.

The emergence of Γ_n as a critical factor in determining the spatiotemporal variability of the surface wind stress response to mesoscale SST variability is one of the main results of this analysis. To characterize the patterns of its spatial and temporal variability, we computed empirical orthogonal functions (EOFs) of Γ_n for each region (Fig. 18). The dominant EOF accounts for more than 80%

and 50% of the variance in the Northern and Southern Hemisphere regions, respectively. This first mode describes coherent seasonal variability, where Γ_n waxes during winter and wanes during summer, following the seasonal cycle of the large-scale ENW. The amplitude of the Γ_n seasonal cycle is largest over the Kuroshio and North Atlantic (NATL) where seasonal variations of the large-scale winds are strongest.

The normalized spatial mode of Γ_n varies mainly between 0.4 and 1 (middle column, Fig. 18), revealing that the amplitude of the seasonal pulsing of Γ_n varies by more

than a factor of 2 within each region. Over the Kuroshio, the amplitude of the seasonal variability of Γ_n is the greatest of all four regions considered here, consistent with the large seasonal pulsing of α_τ observed there in Fig. 9. Over the North Atlantic, the seasonal cycle strengthens from the nearshore region off the eastern coast of North America to a maximum 500–1000 km offshore. In the South Atlantic, the maximum occurs east of the Zapiola gyre center, decreasing to about 0.3 near the confluence of the Brazil and Malvinas currents. Over the Agulhas Return Current, a maximum occurs downstream of the Kerguelen Plateau located near 45°S, 75°E, then decreasing to about 0.3 near the South African coast and the Agulhas Retroflection region and to nearly zero north of 30°S.

The magnitudes of the seasonal variations of Γ_n evident in these EOFs are significant fractions of the 7-yr mean Γ_n fields over all four regions (left column, Fig. 18). The time mean Γ_n is largest over the Agulhas Return Current and smallest over the Kuroshio, with differences between the two regions exceeding a factor of 2. The map of α_τ in Fig. 15 largely mirrors the salient features of the time-averaged Γ_n, although as Eq. (8) infers, geographic variations of α_{vn} also contribute to spatial variations between Γ_n and α_τ.

Finally, the second term on the rhs of Eq. (6) also contributes to the seasonal pulsing of the SST-induced wind stress perturbations through β_τ, albeit to a much lesser extent than the term associated with Γ_n. Over the Kuroshio and North Atlantic, β_τ is largest during winter and nearly vanishes during summer (purple curves, Fig. 17). Over the South Atlantic and Agulhas Return Current, β_τ has a less pronounced seasonal cycle, although there is evidence of a slight wintertime enhancement. Enhancement of β_τ during midlatitude winter is consistent with the increased frequency of high wind events during winter over warm SST perturbations found by Sampe and Xie (2007), providing additional evidence to support that β_τ is associated with SST-induced modulation of transient high wind events.

5. Summary and conclusions

The interrelationships between the surface wind stress, 10-m equivalent neutral wind (ENW), and SST perturbations on oceanic mesoscales were identified over four midlatitude regions with strong SST frontal zones: the Kuroshio Extension, North and South Atlantic, and the Agulhas Return Current. Despite the nonlinear dependence between the surface stress and ENW, spatially high-pass-filtered perturbations of both were shown empirically to be linearly related to the spatially high-pass-filtered SST perturbations. It was shown that an analytical

relationship exists between the separate linear relations for stress and ENW; the stress magnitude perturbations were linearized in terms of the ENW perturbations multiplied by a nonlinear function Γ_n of the ambient large-scale ENW. The stress response to SST can thus be specified in terms of the ENW response to SST and the ambient large-scale ENW.

Relating the responses of the wind stress magnitude and ENW to SST clarifies their interrelationships, while yielding new insights into the influence of mesoscale SST perturbations on the surface wind stress. It was shown that seasonal variability of the ambient large-scale ENW causes a large-amplitude seasonal pulsing of the SST-induced surface stress perturbations, which are several times stronger during winter compared to summer. This seasonal pulsing of the mesoscale stress perturbations is caused by nonlinear amplification of the SST-induced ENW perturbations by the seasonally-varying ambient large-scale ENW. Similarly, geographical variability of the ambient large-scale ENW causes significant variability in the surface stress response to SST.

These results imply a potentially significant source of seasonally varying forcing on the ocean circulation that has not been generally incorporated in numerical models of wind-forced ocean circulation. The seasonal pulsing of the surface stress response to SST also implies that the response of the atmospheric boundary layer to mesoscale SST variability also experiences significant seasonal variations; this can be accomplished, for instance, by a seasonally varying response of the vertically integrated pressure to SST. An extension of this analysis to the SST-induced responses of the wind stress curl and divergence will be described in a forthcoming paper.

APPENDIX A

Sensitivity of Coupling Coefficient Estimates

The sensitivity of the calculations of α_τ and α_{vn} to satellite dataset and neutral drag coefficient are assessed.

a. α_{vn} estimates from other datasets

In this paper, the coupling coefficient α_{vn} estimated from the QuikSCAT ENW and AMSR-E SST fields was used as the primary means of quantifying the ENW response to SST on the oceanic mesoscale. For comparison, we also show α_{vn} estimates computed from three additional combinations of independent data sources: the AMSR-E ENW and AMSR-E SST; the WindSat ENW and SST (version 7 from RSS); and the QuikSCAT ENW and SST from the Reynolds OI v2 SST analyses (from the 0.25°, AVHRR-only dataset). All datasets were gridded onto the same 0.25° spatial grid, have similar spatial resolutions of $O(25–50 \text{ km})$, and have a homogeneous data record over the 7-yr analysis period considered here. Binned scatterplots of the spatially high-pass-filtered ENW as a function of the spatially high-pass-filtered SST are shown in Fig. A1 for the four analysis regions. The α_{vn} estimates are very similar over all regions, differing by less than 10% between all dataset versions.

The values of α_{vn} from the various dataset combinations are summarized in Table A1. Also listed are the values of α_{vn} obtained from previous versions of the QuikSCAT ENW (RSS version 3) and the AMSR-E SST (RSS version 5). These earlier versions were used, for instance, in O'Neill et al. (2010a), whose values of α_{vn} are between 5%–10% larger than those found here (the regions used in that study also differ somewhat in size than the regions used here, which contributes to some of the differences between that study and this one). The coupling coefficient differences between the RSS QuikSCAT versions 3 and 4 datasets are caused by an ENW correction for ENW speeds greater than 15 m s^{-1} applied to version 4 wind speeds; above this threshold, the version 4 ENW speeds are significantly reduced compared to those from version 3 (L. Ricciardulli and F. Wentz 2012, personal communication). We have verified this conclusion through direct computation and also found that the upgraded AMSR-E SST dataset did not contribute to any differences in the coupling coefficient estimates (not shown).

Time series of α_{vn} computed from these three combinations of satellite-based datasets are shown in Fig. A2 for the four regions. The temporal variability of the α_{vn} estimates is similar for all datasets, with overall differences not exceeding 10%.

From this analysis, we thus conclude that the coupling between ENW and SST on the oceanic mesoscale is a feature common to a variety of independent satellite-based ENW and SST fields, and that estimates of α_{vn} do not appear sensitive to satellite dataset.

b. Sensitivity of α_τ to choice of neutral drag coefficient

We assess the sensitivity of this analysis on the specifications of the neutral drag coefficient and surface air density on the QuikSCAT wind stress response to the AMSR-E SST perturbations. Figure A3 shows binned scatterplots of the spatially high-pass-filtered QuikSCAT wind stress magnitude as a function of the spatially high-pass-filtered AMSR-E SST over the Agulhas Return Current and North Atlantic regions computed 4 different ways. The first uses the COARE neutral drag coefficient and a spatially and temporally constant air density. The second is based on the COARE neutral drag coefficient and an air density computed from the National Centers for Environmental Prediction (NCEP) FNL 6-hourly analyses, which was interpolated in space and time to the individual QuikSCAT ENW measurements within each swath over the 7-yr analysis period. The third method uses the neutral drag coefficient specified by Large et al. (1994) most commonly used in estimating wind stress from scatterometer ENWs and a constant air density. The Large et al. (1994) formulation takes the same form as Eq. (2), but with coefficients of $a_0 = 2.70 \times 10^{-3}$ m s^{-1}, $b_0 = 0.142 \times 10^{-3}$, and $c_0 = 0.0764 \times 10^{-3}$ m^{-1} s. The fourth method uses a constant drag coefficient of $C_{d10n} = 1.5 \times 10^{-3}$ [which, in terms of Eq. (2), has coefficients of $a_0 = 0$ m s^{-1}, $b_0 = 1.5 \times 10^{-3}$, and $c_0 = 0$ m^{-1} s] and a constant surface air density.

As shown in Fig. A3, the different air densities have a virtually indistinguishable effect on α_τ, while α_τ from COARE is about 10%–15% larger than those estimated from the stress using the Large et al. (1994) neutral drag coefficient over both regions. Estimates of α_τ using the stress computed from the constant C_{d10n} are about 20% smaller than those computed from the wind stresses with the COARE C_{d10n}. Time series of α_τ for these two regions using the 4 different methods for estimating the stress also show similar results, as shown in Fig. A4. Virtually no difference is found using the different air densities, but α_τ from the QuikSCAT stresses using the COARE drag coefficient were somewhat larger than that from Large et al. (1994). The constant drag coefficient produces smaller estimates of α_τ. Additionally, the seasonal variations of α_τ are similar using any of the three drag coefficient specifications, although the wintertime enhancement of α_τ is slightly less pronounced using the constant C_{d10n}.

The case of a constant drag coefficient was shown, not because it is physically plausible, but to demonstrate the relative insensitivity of the variability of the SST-induced stress perturbations to the specification of the neutral drag
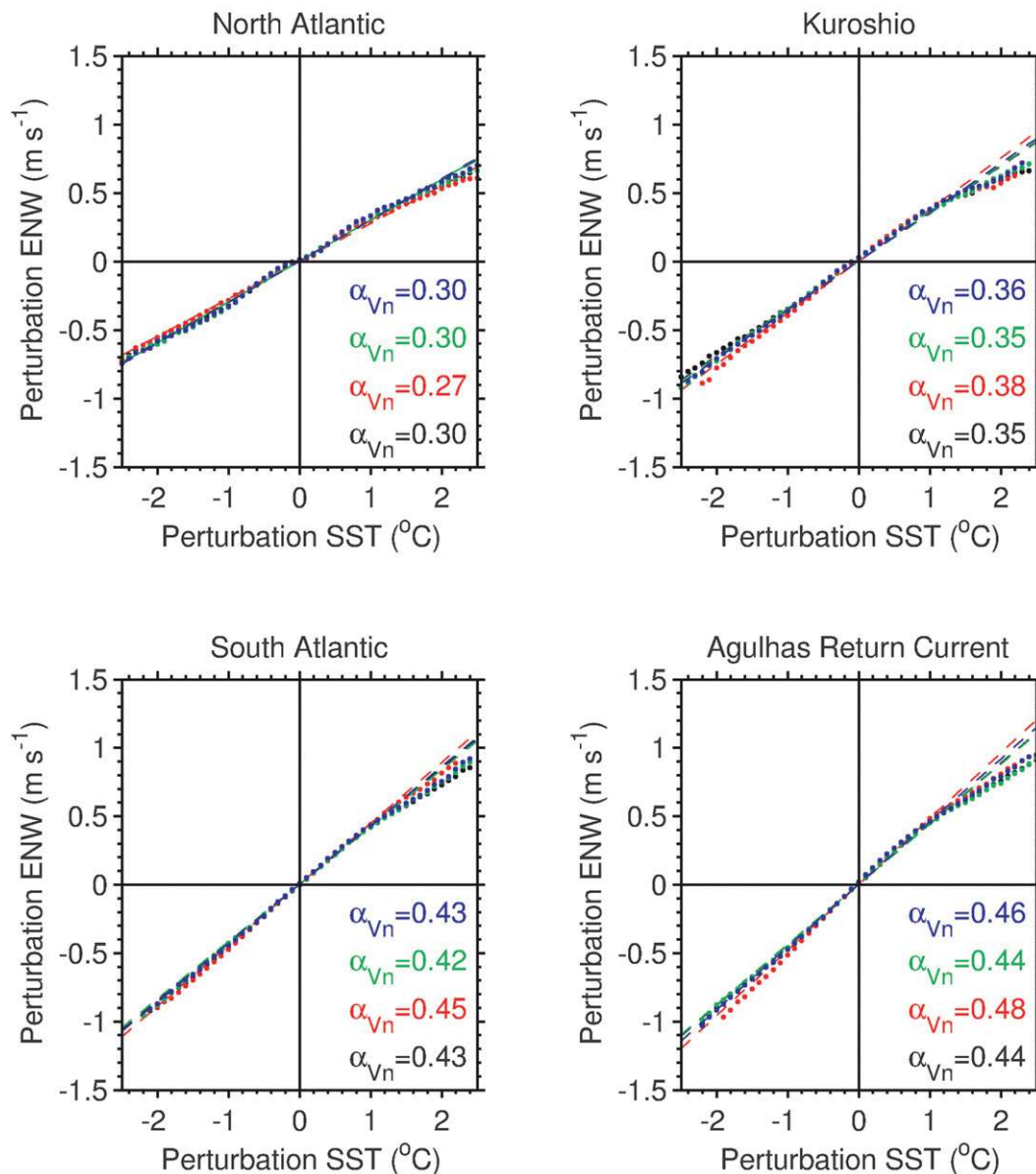
FIG. A1. Binned scatterplots of the spatially high-pass-filtered ENW perturbations as a function of the spatially pass-filtered SST perturbations computed from the WindSat ENW/SST (blue), AMSR-E ENW/SST (green), QuikSCAT ENW/Reynolds OI-v2 AVHRR-only SST (red), and the QuikSCAT ENW/AMSR-E SST combination used throughout this analysis (black). The points represent the mean perturbation ENW within each perturbation SST bin. The units of the α_{vn}'s listed in the panels are m s^{-1} °C^{-1}. The dashed lines are based on linear least squares regressions of the points in each bin.

TABLE A1. Values of α_{vn} computed from the ENW and SST datasets listed in the left columns as discussed in the text. The units of α_{vn} are in m s^{-1} °C^{-1}.

ENW	SST	N. Atlantic	Kuroshio	S. Atlantic	Agulhas
QuikSCAT v4	AMSR-E v7	0.30	0.35	0.43	0.44
QuikSCAT v3	AMSR-E v5	0.32	0.37	0.44	0.47
WindSat v7	WindSat v7	0.30	0.36	0.43	0.46
AMSR-E v7	AMSR-E v7	0.30	0.35	0.42	0.44
QuikSCAT v4	Reynolds OI-v2	0.27	0.38	0.45	0.48

coefficient. This sensitivity analysis shows that qualitatively similar results are obtained using three different neutral drag coefficient parameterizations. The results of this analysis are thus not contingent on a particular form of the drag coefficient.

Since the COARE drag coefficient is based on a much larger and more up-to-date dataset of turbulence measurements, we decided to use the COARE drag coefficient for our analysis. Additionally, the COARE flux algorithm in general is becoming widely used in the air–sea interaction and numerical weather prediction communities, and the results presented here are more comparable with these analyses. It should be noted that the accuracies of these neutral drag coefficient parameterizations make it difficult to objectively distinguish between many of the different parameterizations that have been proposed. In any event,

FIG. A2. Time series of α_{vn} computed from the spatially high-pass-filtered ENW and SST fields at monthly intervals: WindSat ENW/SST (blue), AMSR-E ENW/SST (green), QuikSCAT ENW/Reynolds OI-v2 AVHRR-only SST (red), and the QuikSCAT ENW/AMSR-E SST combination used throughout this analysis (black).
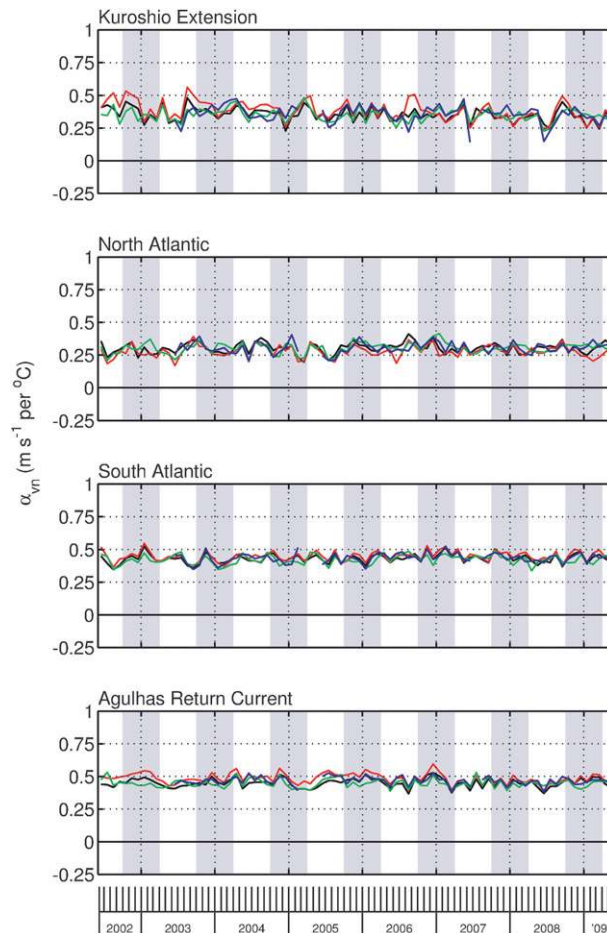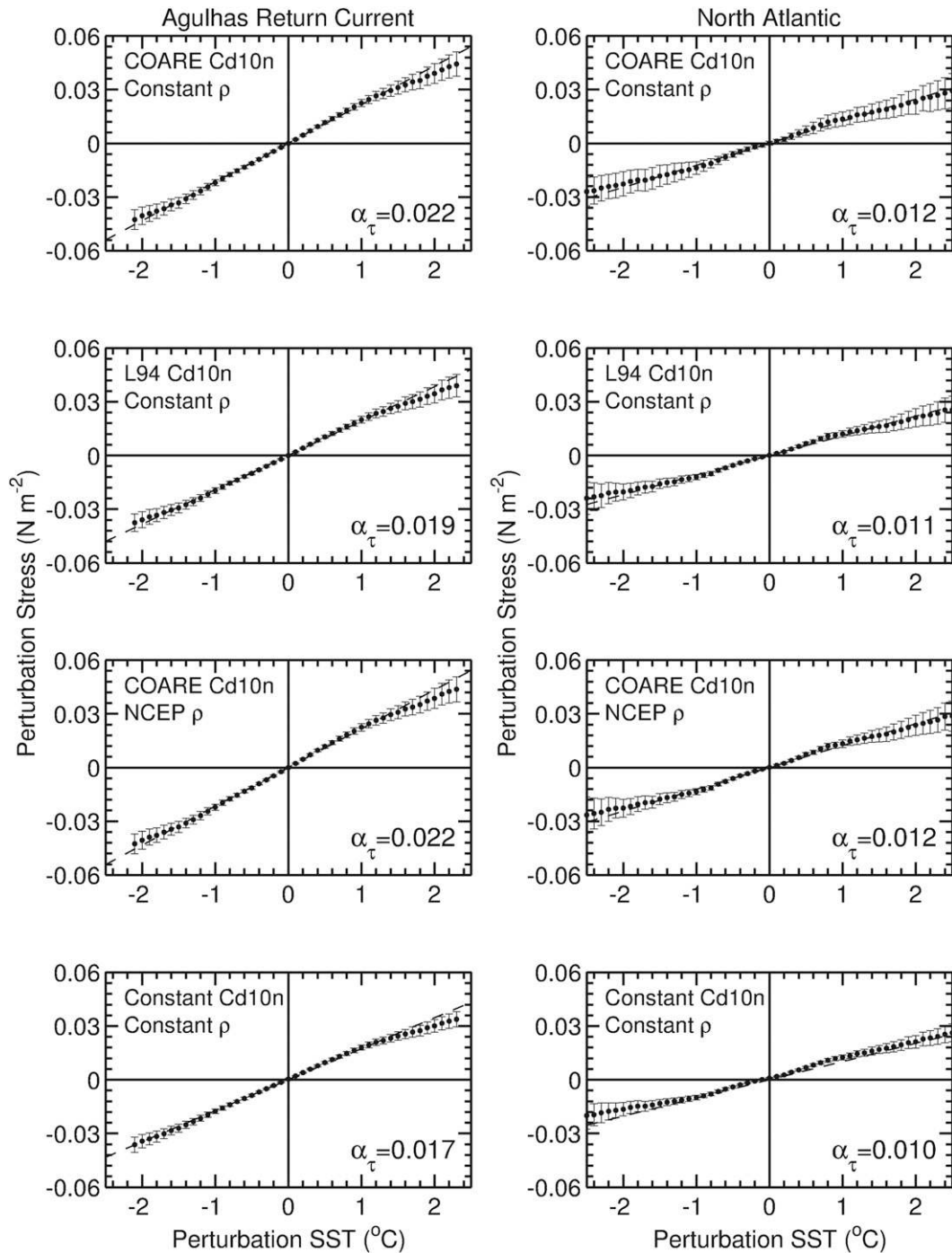
FIG. A3. Binned scatterplots of the QuikSCAT perturbation wind stress as a function of the AMSR-E SST, computed using various methods over (left) the Agulhas Return Current and (right) North Atlantic. Using the QuikSCAT wind stress magnitude from the following: (top) the COARE drag coefficient approximation from Eq. (2) based on Fairall et al. (2003) and a constant surface air density (the method used in this analysis); (second row) the Large et al. (1994) neutral drag coefficient and a constant air density; (third row) the COARE neutral drag coefficient and a variable air density estimated from the NCEP FNL $1 \times 1°$ analyses fields; and (bottom) a constant neutral drag coefficient of 1.5×10^{-3} and a constant air density. The mean values in each bin are shown by the points and the error bars represent the 95% confidence intervals of the mean within each bin.
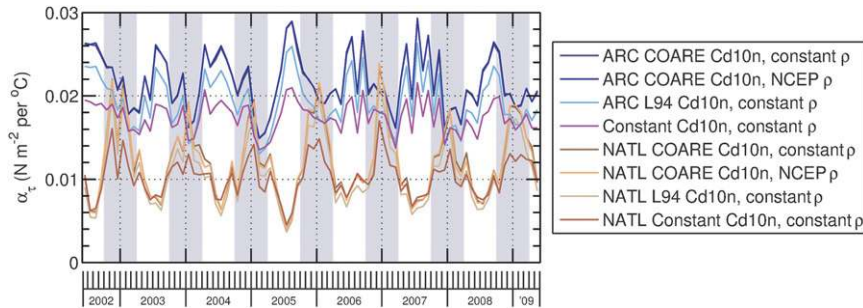
FIG. A4. Time series of α_τ computed from the various estimates of the perturbation QuikSCAT surface wind stress magnitude over the ARC and the NATL. Shown are the QuikSCAT stress estimates using the COARE neutral drag coefficient (Fairall et al. 2003), the Large et al. (1994) neutral drag coefficient using a constant air density, the COARE neutral drag coefficient with a spatially and temporally varying air density estimated from the NCEP FNL analyses, and using a constant neutral drag coefficient and constant air density.

the results of our analysis are not dependent upon any particular neutral drag coefficient parameterization.

APPENDIX B

Derivation of Spatially Filtered Stress–ENW Relationship

An analytical relationship between the time-averaged and spatially filtered wind stress magnitude $\overline{|\tau|}'$ in terms of the ENW $\overline{V_n}'$ is sought to understand the relationships observed in section 3 between the stress and ENW responses to SST. To find such a relationship, first consider V_n partitioned into time-averaged $\overline{V_n}$ and time-varying V_n^* components so that $V_n = \overline{V_n} + V_n^*$ and $\overline{V_n^*} = 0$. Substituting this into Eq. (3) gives

$$\frac{|\tau|}{\rho_0} = a_0(\overline{V_n} + V_n^*) + b_0(\overline{V_n} + V_n^*)^2 + c_0(\overline{V_n} + V_n^*)^3$$

$$= a_0(\overline{V_n} + V_n^*) + b_0(\overline{V_n}^2 + 2\overline{V_n}V_n^* + V_n^{*2})$$

$$+ c_0(\overline{V_n}^3 + 3\overline{V_n}^2 V_n^* + 3\overline{V_n}V_n^{*2} + V_n^{*3}).$$

Taking the time average of $|\tau|$ yields, after rearrangement,

$$\frac{\overline{|\tau|}}{\rho_0} = (a_0\overline{V_n} + b_0\overline{V_n}^2 + c_0\overline{V_n}^3)$$

$$+ [(b_0 + 3c_0\overline{V_n})\overline{V_n^{*2}} + c_0\overline{V_n^{*3}}]. \quad (B1)$$

Spatial filtering is introduced in a similar manner by first decomposing the time-averaged $\overline{V_n}$ into a large-scale ENW $\widetilde{\overline{V_n}}$ corresponding to the spatially low-pass-filtered ENW field, and a perturbation ENW $\overline{V_n}'$

corresponding to the spatially high-pass-filtered ENW field such that $\overline{V_n} = \widetilde{\overline{V_n}} + \overline{V_n}'$ and $\widetilde{\overline{V_n}'} = 0$. The first term on the rhs of Eq. (A1) can then be expressed as[B1]

$$(a_0\overline{V_n} + b_0\overline{V_n}^2 + c_0\overline{V_n}^3)$$

$$= a_0\left(\widetilde{\overline{V_n}} + \overline{V_n}'\right) + b_0\left(\widetilde{\overline{V_n}}^2 + 2\widetilde{\overline{V_n}}\,\overline{V_n}' + \overline{V_n}'^2\right)$$

$$+ c_0\left(\widetilde{\overline{V_n}}^3 + 3\widetilde{\overline{V_n}}^2\overline{V_n}' + 3\widetilde{\overline{V_n}}\,\overline{V_n}'^2 + \overline{V_n}'^3\right).$$

Simple rearrangement of terms yields

$$(a_0\overline{V_n} + b_0\overline{V_n}^2 + c_0\overline{V_n}^3) = (a_0 + 2b_0\widetilde{\overline{V_n}} + 3c_0\widetilde{\overline{V_n}}^2)\overline{V_n}'$$

$$+ (b_0 + 3c_0\widetilde{\overline{V_n}})\overline{V_n}'^2 + c_0\overline{V_n}'^3$$

$$+ a_0\widetilde{\overline{V_n}} + b_0\widetilde{\overline{V_n}}^2 + c_0\widetilde{\overline{V_n}}^3.$$

Spatial high-pass filtering this equation removes the spatially low-pass-filtered wind speed components $\widetilde{\overline{V_n}}$, $\widetilde{\overline{V_n}}^2$, and $\widetilde{\overline{V_n}}^3$ that do not multiply any powers of the spatially high-pass-filtered wind components, leaving

$$(a_0\overline{V_n} + b_0\overline{V_n}^2 + c_0\overline{V_n}^3)' = (a_0 + 2b_0\widetilde{\overline{V_n}} + 3c_0\widetilde{\overline{V_n}}^2)\overline{V_n}'$$

$$+ (b_0 + 3c_0\widetilde{\overline{V_n}})\overline{V_n}'^2 + c_0\overline{V_n}'^3.$$

Combining this with the spatially high-pass-filtered second term on the rhs of Eq. (A1) yields an analytical

---

[B1] Note that the loess spatial high-pass filter used here behaves as a linear operator, thus allowing commutation of the time averaging and spatial filtering operations.

expression for the time-averaged and spatially filtered surface wind stress magnitude $\overline{|\tau|}'$,

$$\frac{\overline{|\tau|}'}{\rho_0} = \left(a_0 + 2b_0\widetilde{\overline{V_n}} + 3c_0\widetilde{\overline{V_n}}^2\right)\overline{V_n}' + \left(b_0 + 3c_0\widetilde{\overline{V_n}}\right)\overline{V_n}'^2$$
$$+ c_0\overline{V_n}'^3 + \left[(b_0 + 3c_0\overline{V_n})\overline{V_n^{*2}} + c_0\overline{V_n^{*3}}\right]'.$$

This expression can be simplified by noting that, for typical values of $\overline{V_n}' = 1$ m s^{-1}, and $\widetilde{\overline{V_n}} = 7$ m s^{-1}, the first term on the rhs contributes 89.8% to the total perturbation stress; the term $c_0\overline{V_n}'^3$ contributes only 0.4% to the perturbation stress; and the term $(b_0 + 3c_0\overline{V_n})\overline{V_n}'^2$ contributes 9.8%. Additionally, $(b_0 + 3c_0\overline{V_n})\overline{V_n}'^2$ does not affect α_τ appreciably since a binned scatterplot of $\overline{V_n}'^2$ as a function of $\overline{T_s}'$ is a parabola with its vertex at the origin (since $\overline{V_n}'$ varies empirically as a linear function of $\overline{T_s}'$); fitting a line through such a parabola gives a near-zero slope. The term containing $\overline{V_n}'^2$ thus has a very small effect on the perturbation wind stress response to SST. For this reason and because of their small effect on the perturbation stress, the quantities with higher-order powers of $\overline{V_n}'$ are neglected, leaving

$$\overline{|\tau|}' \approx \rho_0\left(a_0 + 2b_0\widetilde{\overline{V_n}} + 3c_0\widetilde{\overline{V_n}}^2\right)\overline{V_n}'$$
$$+ \rho_0\left[(b_0 + 3c_0\overline{V_n})\overline{V_n^{*2}} + c_0\overline{V_n^{*3}}\right]'. \quad (B2)$$

This is the form used in this analysis. We note that the terms containing V_n^{*2} and V_n^{*3} are very difficult to compute directly. Fortunately, these terms can be simplified into more computationally tractable quantities by first noting that V_n^{*2} may be solved for from the following expression,

$$V_n^2 = (\overline{V_n} + V_n^*)^2 = \overline{V_n}^2 + 2\overline{V_n}V_n^* + V_n^{*2}$$

to yield

$$V_n^{*2} = V_n^2 - \overline{V_n}^2 - 2\overline{V_n}V_n^*.$$

Taking the time average of this gives

$$\overline{V_n^{*2}} = \overline{V_n^2} - \overline{V_n}^2,$$

which does not have explicit dependence on the time-varying wind speed V_n^*. Similarly, V_n^{*3} can be rewritten by noting that

$$V_n^3 = (\overline{V_n} + V_n^*)^3 = \overline{V_n}^3 + 3\overline{V_n}^2V_n^* + 3\overline{V_n}V_n^{*2} + V_n^{*3},$$

so that

$$V_n^{*3} = V_n^3 - 3\overline{V_n}^2V_n^* - 3\overline{V_n}V_n^{*2} - \overline{V_n}^3,$$

leading to

$$\overline{V_n^{*3}} = \overline{V_n^3} - 3\overline{V_n}\overline{V_n^{*2}} - \overline{V_n}^3.$$

Substituting for $\overline{V_n^{*2}}$ from above, the terms in the square braces on the rhs of Eq. (A2) become

$$\left[(b_0 + 3c_0\overline{V_n})\overline{V_n^{*2}} + c_0\overline{V_n^{*3}}\right]' = b_0(\overline{V_n^2}' - \overline{V_n}^{2'})$$
$$+ c_0(\overline{V_n^3}' - \overline{V_n}^{3'}).$$

All of the terms on the rhs of this equation are thus expressible in terms of time averages of the first, second, or third moments of the total ENW V_n and the time-varying ENW $\overline{V_n^*}$ thus does not need to be computed directly, which greatly simplifies the analysis.

REFERENCES

Anderson, S. P., 2001: On the atmospheric boundary layer over the equatorial front. *J. Climate,* **14,** 1688–1695.

Bendat, J. S., and A. G. Piersol, 1986: *Random Data Analysis and Measurement Procedures.* 2nd ed. Wiley & Sons, 566 pp.

Bond, N. A., 1992: Observations of planetary boundary layer structure in the eastern equatorial Pacific. *J. Climate,* **5,** 699–706.

Bourassa, M. A., D. G. Vincent, and W. L. Wood, 1999: A flux parameterization including the effects of capillary waves and sea state. *J. Atmos. Sci.,* **56,** 1123–1139.

——, D. M. Legler, J. J. O'Brien, and S. R. Smith, 2003: SeaWinds validation with research vessels. *J. Geophys. Res.,* **108,** 3019, doi:10.1029/2001JC001028.

Bourras, D., G. Reverdin, H. Giordani, and G. Caniaux, 2004: Response of the atmospheric boundary layer to a mesoscale oceanic eddy in the northeast Atlantic. *J. Geophys. Res.,* **109,** D18114, doi:10.1029/2004JD004799.

Cayan, D. R., 1992: Latent and sensible heat flux anomalies over the northern oceans: Driving the sea surface temperature. *J. Phys. Oceanogr.,* **22,** 859–881.

Chelton, D. B., 2005: The impact of SST specification on ECMWF surface wind stress fields in the eastern tropical Pacific. *J. Climate,* **18,** 530–550.

——, and M. G. Schlax, 2003: The accuracies of smoothed sea surface height fields constructed from tandem altimeter datasets. *J. Atmos. Oceanic Technol.,* **20,** 1276–1302.

——, and M. H. Freilich, 2005: Scatterometer-based assessment of 10-m wind analyses from the operational ECMWF and NCEP numerical weather prediction models. *Mon. Wea. Rev.,* **133,** 409–429.

——, and S.-P. Xie, 2010: Coupled ocean-atmosphere interaction at oceanic mesoscales. *Oceanogr. Mag.,* **4,** 52–69.

——, and Coauthors, 2001: Observations of coupling between surface wind stress and sea surface temperature in the eastern tropical Pacific. *J. Climate,* **14,** 1479–1498.

Cleveland, W. S., and S. J. Devlin, 1988: Locally weighted regression: An approach to regression analysis by local fitting. *J. Amer. Stat. Assoc.,* **83,** 596–610.

Crombie, D. D., 1955: Doppler spectrum of sea echo at 13.56 mc/s. *Nature,* **175,** 681–682.

Cronin, M. F., S.-P. Xie, and H. Hashizume, 2003: Barometric pressure variations associated with eastern Pacific tropical instability waves. *J. Climate,* **16,** 3050–3057.

de Szoeke, S. P., and C. S. Bretherton, 2004: Quasi-Lagrangian large eddy simulations of cross-equatorial flow in the east Pacific atmospheric boundary layer. *J. Atmos. Sci.,* **61,** 1837–1858.

Ebuchi, N., H. C. Graber, and M. J. Caruso, 2002: Evaluation of wind vectors observed by QuikSCAT/SeaWinds using ocean buoy data. *J. Oceanic Atmos. Technol.,* **19,** 2049–2062.

Fairall, C. W., E. F. Bradley, J. E. Hare, A. A. Grachev, and J. B. Edson, 2003: Bulk parameterization of air–sea fluxes: Updates and verification for the COARE algorithm. *J. Climate,* **16,** 571–591.

Frankignoul, C., 1985: Sea surface temperature anomalies, planetary waves, and air-sea feedback in midlatitudes. *Rev. Geophys.,* **23,** 357–390.

Friehe, C. A., and Coauthors, 1991: Air-sea fluxes and surface layer turbulence around a sea surface temperature front. *J. Geophys. Res.,* **96** (C5), 8593–8609.

Garratt, J. R., 1977: Review of drag coefficients over oceans and continents. *Mon. Wea. Rev.,* **105,** 915–929.

Geernaert, G., 1990: Bulk parameterizations for the wind stress and heat flux. *Surface Waves and Fluxes: Theory and Remote Sensing,* Vol. 1, G. Geernaert and W. Plant, Eds., Kluwer Academic, 91–172.

Haack, T., D. Chelton, J. Pullen, J. D. Doyle, and M. Schlax, 2008: Summertime influence of SST on surface wind stress off the U.S. west coast from the U.S. Navy COAMPS model. *J. Phys. Oceanogr.,* **38,** 2414–2437.

Hashizume, H., S.-P. Xie, W. T. Liu, and K. Takeuchi, 2001: Local and remote atmospheric response to tropical instability waves: A global view from space. *J. Geophys. Res.,* **106** (D10), 10 173–10 185.

——, ——, M. Fujiwara, M. Shiotani, T. Watanabe, Y. Tanimoto, W. T. Liu, and K. Takeuchi, 2002: Direct observations of atmospheric boundary layer response to SST variations associated with tropical instability waves over the eastern equatorial Pacific. *J. Climate,* **15,** 3379–3393.

Hayes, S. P., M. J. McPhaden, and J. M. Wallace, 1989: The influence of sea surface temperature on surface wind in the eastern equatorial Pacific. *J. Climate,* **2,** 1500–1506.

Hogg, A. C. M., W. K. Dewar, P. Berloff, S. Kravtsov, and D. K. Hutchinson, 2009: The effects of mesoscale ocean–atmosphere coupling on the large-scale ocean circulation. *J. Climate,* **22,** 4066–4082.

Jin, X., C. Dong, J. Kurian, J. C. McWilliams, D. B. Chelton, and Z. Li, 2009: Wind–SST interaction in coastal upwelling: Oceanic simulation with empirical coupling. *J. Phys. Oceanogr.,* **39,** 2957–2970.

Jones, W. L., and L. C. Schroeder, 1978: Radar backscatter from the ocean: Dependence on surface friction velocity. *Bound.-Layer Meteor.,* **13,** 133–149.

Jury, M. R., 1994: Thermal front within the marine atmospheric boundary layer over the Agulhas Current south of Africa: Composite aircraft observations. *J. Geophys. Res.,* **99** (C2), 3297–3304.

——, and N. Walker, 1988: Marine boundary layer modification across the edge of the Agulhas Current. *J. Geophys. Res.,* **93** (C1), 647–654.

Kudryavtsev, V. N., S. A. Grodsky, V. A. Dulov, and V. V. Malinovsky, 1996: Observations of atmospheric boundary layer evolution above the Gulf Stream frontal zone. *Bound.-Layer Meteor.,* **79,** 51–82.

Kwon, B. H., B. Bénech, D. Lambert, P. Durand, A. Druilhet, H. Giordani, and S. Planton, 1998: Structure of the marine atmospheric boundary layer over an oceanic thermal front: SEMAPHORE experiment. *J. Geophys. Res.,* **103** (C11), 25 159–25 180.

Large, W. G., J. C. McWilliams, and S. C. Doney, 1994: Oceanic vertical mixing: A review and a model with a nonlocal boundary layer parameterization. *Rev. Geophys.,* **32,** 363–403.

——, J. Morzel, and G. B. Crawford, 1995: Accounting for surface wave distortion of the marine wind profile in low-level Ocean Storms wind measurements. *J. Phys. Oceanogr.,* **25,** 2959–2971.

Li, F., W. Large, W. Shaw, E. J. Walsh, and K. Davidson, 1989: Ocean radar backscatter relationship with near-surface winds: A case study during FASINEX. *J. Phys. Oceanogr.,* **19,** 342–353.

Lindzen, R. S., and S. Nigam, 1987: On the role of sea surface temperature gradients in forcing low-level winds and convergence in the tropics. *J. Atmos. Sci.,* **44,** 2418–2436.

Liu, W. T., and W. Tang, 1996: Equivalent neutral wind. JPL Publication 96–17, 16 pp.

——, and X. Xie, 2008: Ocean–atmosphere momentum coupling in the Kuroshio Extension observed from space. *J. Oceanogr.,* **64,** 631–637.

——, ——, P. S. Polito, S.-P. Xie, and H. Hashizume, 2000: Atmospheric manifestation of tropical instability waves observed by QuikSCAT and Tropical Rain Measuring Mission. *Geophys. Res. Lett.,* **27,** 2545–2548.

——, ——, and P. Niiler, 2007: Ocean–atmosphere interaction over Agulhas Extension meanders. *J. Climate,* **20,** 5784–5797.

Mahrt, L., D. Vickers, and E. Moore, 2004: Flow adjustments across sea surface temperature changes. *Bound.-Layer Meteor.,* **111,** 553–564.

Maloney, E. D., and D. B. Chelton, 2006: An assessment of the sea surface temperature influence on surface wind stress in numerical weather prediction and climate models. *J. Climate,* **19,** 2743–2762.

Mantua, N. J., S. R. Hare, Y. Zhang, J. M. Wallace, and R. C. Francis, 1997: A Pacific interdecadal climate oscillation with impacts on salmon production. *Bull. Amer. Meteor. Soc.,* **78,** 1069–1079.

Mey, R. D., N. D. Walker, and M. R. Jury, 1990: Surface heat fluxes and marine boundary layer modification in the Agulhas Retroflection region. *J. Geophys. Res.,* **95** (C9), 15 997–16 015.

Milliff, R. F., W. G. Large, W. R. Holland, and J. C. McWilliams, 1996: The general circulation responses of high-resolution North Atlantic Ocean models to synthetic scatterometer winds. *J. Phys. Oceanogr.,* **26,** 1747–1768.

Minobe, S., A. Kuwano-Yoshida, N. Komori, S.-P. Xie, and R. J. Small, 2008: Influence of the Gulf Stream on the troposphere. *Nature,* **452,** 206–209.

Mitsuyasu, H., and T. Honda, 1974: The high frequency spectrum of wind-generated waves. *J. Oceanogr. Soc. Japan,* **30,** 185–198.

Nonaka, M., and S.-P. Xie, 2003: Covariations of sea surface temperature and wind over the Kuroshio and its extension: Evidence for ocean–to–atmosphere feedback. *J. Climate,* **16,** 1404–1413.

O'Neill, L. W., 2012: Wind speed and stability effects on the coupling between surface wind stress and SST observed from buoys and satellite. *J. Climate,* **25,** 1544–1569.

——, D. B. Chelton, and S. K. Esbensen, 2003: Observations of SST-induced perturbations on the wind stress field over the Southern Ocean on seasonal timescales. *J. Climate,* **16,** 2340–2354.

——, ——, ——, and F. J. Wentz, 2005: High-resolution satellite measurements of the atmospheric boundary layer response to SST perturbations over the Agulhas Return Current. *J. Climate,* **18,** 2706–2723.

——, ——, and ——, 2010a: The effects of SST-induced surface wind speed and direction gradients on midlatitude surface vorticity and divergence. *J. Climate,* **23,** 255–281.

——, S. K. Esbensen, N. Thum, R. M. Samelson, and D. B. Chelton, 2010b: Dynamical analysis of the boundary layer and surface wind responses to mesoscale SST perturbations. *J. Climate,* **23,** 559–581.

Okumura, Y., S.-P. Xie, A. Numaguti, and Y. Tanimoto, 2001: Tropical Atlantic air–sea interaction and its influence on the NAO. *Geophys. Res. Lett.,* **28,** 1507–1510.

Orlanski, I., 1975: A rational subdivision of scales for atmospheric processes. *Bull. Amer. Meteor. Soc.,* **56,** 527–530.

Park, K.-A., and P. C. Cornillon, 2002: Stability-induced modification of sea surface winds over Gulf Stream rings. *Geophys. Res. Lett.,* **29,** 2211, doi:10.1029/2001GL014236.

——, ——, and D. L. Codiga, 2006: Modification of surface winds near ocean fronts: Effects of Gulf Stream rings on scatterometer (QuikSCAT, NSCAT) wind observations. *J. Geophys. Res.,* **111,** C03021, doi:10.1029/2005JC003016.

Pezzi, L. P., J. Vialard, K. J. Richards, C. Menkes, and D. Anderson, 2004: Influence of ocean-atmosphere coupling on the properties of tropical instability waves. *Geophys. Res. Lett.,* **34,** L16306, doi:10.1029/2004GL019995.

——, R. B. Souza, M. S. Dourado, C. A. E. Garcia, M. M. Mata, and M. A. F. Silva-Dias, 2005: Ocean–atmosphere in situ observations at the Brazil–Malvinas confluence region. *Geophys. Res. Lett.,* **32,** L22603, doi:10.1029/2005GL023866.

Pickett, M. H., W. Tang, L. K. Rosenfeld, and C. H. Wash, 2003: QuikSCAT satellite comparisons with near-shore buoy wind data off the U.S. West Coast. *J. Atmos. Oceanic Technol.,* **20,** 1869–1879.

Pierson, W. J., and R. A. Stacy, 1973: The elevation, slope, and curvature spectra of a wind roughened sea surface. NASA Contractor Tech. Rep. CR-2247, 126 pp.

Polito, P. S., J. P. Ryan, W. T. Liu, and F. P. Chavez, 2001: Oceanic and atmospheric anomalies of tropical instability waves. *Geophys. Res. Lett.,* **28,** 2233–2236.

Portabella, M., and A. Stoffelen, 2009: On scatterometer ocean stress. *J. Atmos. Oceanic Technol.,* **26,** 368–382.

Raymond, D. J., and Coauthors, 2004: EPIC2001 and the coupled ocean–atmosphere system of the tropical east Pacific. *Bull. Amer. Meteor. Soc.,* **85,** 1341–1354.

Rice, S. O., 1951: Reflection of electromagnetic waves from slightly rough surfaces. *Commun. Pure Appl. Math.,* **4,** 351.

Risien, C. M., and D. B. Chelton, 2008: A global climatology of surface wind and wind stress fields from eight years of QuikSCAT scatterometer data. *J. Phys. Oceanogr.,* **38,** 2379–2413.

Rogers, D. P., 1989: The marine boundary layer in the vicinity of an ocean front. *J. Atmos. Sci.,* **46,** 2044–2062.

Ross, D. B., V. J. Cardone, J. Overland, R. D. McPherson, W. J. Pierson Jr., and T. Yu, 1985: Oceanic surface winds. *Adv. Geophys.,* **27,** 101–140.

Rouault, M., and J. R. E. Lutjeharms, 2000: Air–sea exchange over an Agulhas eddy at the subtropical convergence. *Global Atmos. Ocean Syst.,* **7,** 125–150.

Samelson, R. M., E. D. Skyllingstad, D. B. Chelton, S. K. Esbensen, L. W. O'Neill, and N. Thum, 2006: On the coupling of wind stress and sea surface temperature. *J. Climate,* **19,** 1557–1566.

Sampe, T., and S.-P. Xie, 2007: Mapping high sea winds from space. *Bull. Amer. Meteor. Soc.,* **88,** 1965–1978.

Schlax, M. G., and D. B. Chelton, 1992: Frequency domain diagnostics for linear smoothers. *J. Amer. Stat. Assoc.,* **87,** 1070–1081.

——, ——, and M. H. Freilich, 2001: Sampling errors in wind fields constructed from single and tandem scatterometer datasets. *J. Atmos. Oceanic Technol.,* **18,** 1014–1036.

Seo, H., A. J. Miller, and J. O. Roads, 2007: The Scripps coupled ocean–atmosphere regional (SCOAR) model, with applications in the eastern Pacific sector. *J. Climate,* **20,** 381–402.

——, R. Murtugudde, M. Jochum, and A. J. Miller, 2008: Modeling of mesoscale coupled ocean-atmosphere interaction and its feedback to ocean in the western Arabian Sea. *Ocean Modell.,* **25** (3–4), 120–131, doi:10.1016/j.ocemod.2008.07.003.

Skyllingstad, E. D., D. Vickers, L. Mahrt, and R. Samelson, 2006: Effects of mesoscale sea surface temperature fronts on the marine atmospheric boundary layer. *Bound.-Layer Meteor.,* **123,** 219–237, doi:10.1007/s10546-006-9127-8.

Small, R. J., S.-P. Xie, and Y. Wang, 2003: Numerical simulation of atmospheric response to Pacific tropical instability waves. *J. Climate,* **16,** 3722–3740.

——, ——, and J. Hafner, 2005a: Satellite observations of mesoscale ocean features and copropagating atmospheric surface fields in the tropical belt. *J. Geophys. Res.,* **110,** C02021, doi:10.1029/2004JC002598.

——, ——, Y. Wang, S. K. Esbensen, and D. Vickers, 2005b: Numerical simulation of boundary layer structure and cross-equatorial flow in the eastern Pacific. *J. Atmos. Sci.,* **62,** 1812–1830.

——, and Coauthors, 2008: Air–sea interaction over ocean fronts and eddies. *Dyn. Atmos. Oceans,* **45,** 274–319, doi:10.1016/j.dynatmoce.2008.01.001.

Song, Q., P. Cornillon, and T. Hara, 2006: Surface wind response to oceanic fronts. *J. Geophys. Res.,* **111,** C12006, doi:10.1029/2006JC003680.

——, D. B. Chelton, S. K. Esbensen, N. Thum, and L. W. O'Neill, 2009: Coupling between sea surface temperature and low-level winds in mesoscale numerical models. *J. Climate,* **22,** 146–164.

Spall, M. A., 2007a: Effect of sea surface temperature–wind stress coupling on baroclinic instability in the ocean. *J. Phys. Oceanogr.,* **37,** 1092–1097.

——, 2007b: Midlatitude wind stress–sea surface temperature coupling in the vicinity of oceanic fronts. *J. Climate,* **20,** 3785–3801.

Sweet, W. R., R. Fett, J. Kerling, and P. LaViolette, 1981: Air–sea interaction effects in the lower troposphere across the north wall of the Gulf Stream. *Mon. Wea. Rev.,* **109,** 1042–1052.

Thum, N., S. K. Esbensen, D. B. Chelton, and M. J. McPhaden, 2002: Air–sea heat exchange along the northern sea surface temperature front in the eastern tropical Pacific. *J. Climate,* **15,** 3361–3378.

Tokinaga, H., Y. Tanimoto, and S.-P. Xie, 2005: SST-induced surface wind variations over the Brazil–Malvinas Confluence: Satellite and in situ observations. *J. Climate,* **18,** 3470–3482.

Vecchi, G. A., S.-P. Xie, and A. S. Fischer, 2004: Ocean–atmosphere covariability in the western Arabian Sea. *J. Climate,* **17,** 1213–1224.

Vihma, T., J. Uotila, and J. Launiainen, 1998: Air-sea interaction over a thermal front in the Denmark Strait. *J. Geophys. Res.,* **103** (C12), 27 665–27 678.

Wai, M., and S. A. Stage, 1989: Dynamical analysis of marine atmospheric boundary layer structure near the Gulf Stream oceanic front. *Quart. J. Roy. Meteor. Soc.,* **115,** 29–44.

Wallace, J. M., T. P. Mitchell, and C. Deser, 1989: The influence of sea surface temperature on surface wind in the eastern equatorial Pacific: Seasonal and interannual variability. *J. Climate,* **2,** 1492–1499.

Weissman, D. E., and H. C. Graber, 1999: Satellite scatterometer studies of ocean surface stress and drag coefficients using a direct model. *J. Geophys. Res.,* **104** (C5), 11 329–11 335.

——, T. W. Thompson, and R. Legeckis, 1980: Modulation of sea surface radar cross section by surface wind stress: Wind speed and air temperature effects across the Gulf Stream. *J. Geophys. Res.,* **85** (C9), 5032–5042.

——, K. L. Davidson, R. A. Brown, C. A. Friehe, and F. Li, 1994: The relationship between microwave radar cross-section and both wind speed and stress: Model function studies using frontal air-sea interaction experiment data. *J. Geophys. Res.,* **99** (C5), 10 087–10 108.

White, W. B., and J. L. Annis, 2003: Coupling of extratropical mesoscale eddies in the ocean to westerly winds in the atmospheric boundary layer. *J. Climate,* **33,** 1095–1107.

Wright, J. W., 1966: Backscattering from capillary waves with application to sea clutter. *IEEE Trans. Antennas Propag.,* **14,** 749–754.

Xie, S.-P., 2004: Satellite observations of cool ocean–atmosphere interaction. *Bull. Amer. Meteor. Soc.,* **85,** 195–208.

——, M. Ishiwatari, H. Hashizume, and K. Takeuchi, 1998: Coupled ocean–atmosphere waves on the equatorial front. *Geophys. Res. Lett.,* **25,** 3863–3866.

Xie, T., W. Perrie, and W. Chen, 2010: Gulf Stream thermal fronts detected by synthetic aperature radar. *Geophys. Res. Lett.,* **37,** L06601, doi:10.1029/2009GL041972.

Xu, H., H. Tokinaga, and S.-P. Xie, 2010: Atmospheric effects of the Kuroshio large meander during 2004/05. *J. Climate,* **23,** 4704–4715.

Zhang, R.-H., and A. J. Busalacchi, 2009: An empirical model for surface wind stress response to SST forcing induced by tropical instability waves (TIWs) in the eastern equatorial Pacific. *Mon. Wea. Rev.,* **137,** 2021–2046.